Theoretical Notes

Note 346

May 1983

MEASUREMENTS OF SWARM PARAMETERS IN DRY AIR

by

D.K. Davies

Westinghouse Electric Corporation

ABSTRACT

This report describes precision measurements of swarm parameters over an extended range of electric field in dry, CO_2-free air. These measurements have been carried out using a pulsed drift tube in which the drift distance is variable to permit differential measurements. The drift tube arrangement is such that the three components of the total drift current due to electrons, negative ions, and positive ions are individually detected. The electron and negative-ion mobilities together with the three-body attachment, two-body attachment, and ionization rates have been determined over the range of E/N (the ratio of electric field to gas density) from 0.6 to 300 x 10^{-21} Vm^2. The present measurements of electron mobility represent the first comprehensive set of measurements in the range of E/N from 10^{-20} to 10^{-19} Vm^2. The values of the three-body attachment rate coefficient determined in the present study lie on the lower edge of the spread of previous measurements. No evidence for either a two-body or a four-body attachment process have been found over the range of E/n from 0.6 to 30 x 10^{-21} Vm^2.

PREFACE

This report was prepared by the Westinghouse R&D Center, 1310 Beulah Road, Pittsburgh, PA 15235, under Subcontract No. DC-SC-2030-1 from Dikewood, Division of Kaman Sciences Corporation, Albuquerque, NM 87102, with C. W. Jones as Project Monitor. The technical effort described in this report was conducted by D. K. Davies. The author is indebted to P. J. Chantry and M. A. Biondi for many fruitful discussions during the course of the work. Thanks are also due to W. M. Uhlig and W. F. Toth for the careful construction of the experimental system and to G. W. Sherwin, T. G. Ketterer, and L. D. Kurtz for their fine technical support. It is also a pleasure to acknowledge many stimulating interactions with C. E. Baum, the Subtask Officer for this work.

TABLE OF CONTENTS

ILLUSTRATIONS

ILLUSTRATIONS CONTINUED

TABLES

I. INTRODUCTION

The determination of air conductivity from air-chemistry models requires a considerable body of basic data concerning the ionization and attachment rates and the transport properties of electrons and ions as a function of electric field. The conductivity σ may be defined by

$$\sigma = e\{n_e \mu_e + \sum_i n_+^i \mu_+^i + \sum_j n_-^j \mu_-^j\} \tag{1}$$

where n_e and μ_e are the electron number density and mobility, respectively, n_+^i and μ_+^i are the positive-ion number density and mobility, respectively, for ions of species i, and n_-^j and μ_-^j are the negative-ion number density and mobility, respectively, for ions of species j. The electron and ion mobilities appear explicitly in Equation (1), whereas the ionization and attachment rates determine, in part, the densities of electrons and ions. Previous knowledge of these parameters in air is either incomplete or subject to large uncertainty, particularly in the case of humid air.

The present study constitutes the initial phase of a program designed to provide a comprehensive set of precision measurements of electron, negative-ion, and positive-ion mobilities together with attachment and ionization coefficients for dry air and mixtures of dry air with water vapor. In this first phase the data determined for dry air are reported. In order to cover the range of electric field encountered during the period of air conductivity following an electromagnetic pulse event, these measurements have been carried out over the range of E/N (the ratio of electric field to gas density) from 6 x 10^{-22} to 3 x 10^{-19} V·m^2. This range of E/N corresponds to values of electric field at atmospheric pressure from ~ 10^4 to ~ 10^7 V/m and covers values of electron mean energy from near thermal to values well above the onset of impact ionization.

II. EXPERIMENTAL PROCEDURE

1. DRIFT TUBE

A sectional drawing of the drift tube chamber is shown in Figure 1 and a photograph of the internal structure in Figure 2. A uniform-field drift region is maintained between the semitransparent cathode and anode by a set of ten annular guard rings 0.16 cm thick having an external diameter of 8.9 cm and internal diameter of 5.1 cm. The guard rings are separated by precision spherical sapphire spacers such that the centers of the rings are accurately spaced 0.5 cm apart. Both anode and cathode are electrically shielded from the drift region by a highly transparent etched grid (Ref. 1) located 0.1 cm from the surface of each electrode. Each grid is 0.0025 cm thick and contains 20 lines/cm with a line thickness of 0.0033 cm giving an optical transparency of 87%.

The cathode consists of a plate with a bevelled sapphire disc insert, 1.6 cm in diameter, centered along the axis of the drift tube and with its surface coplanar with the surface of the plate adjacent to the drift region. The bevelled edge and lip of the sapphire are coated with gold to a thickness of 1400 Å prior to its insertion in the support plate. After assembly, the entire surface of the plate and insert adjacent to the drift region are coated with gold to a thickness of 300 Å. Electrical contact between the thin gold-film photocathode and the support plate is provided through the thicker gold film deposited on the lip and edge of the sapphire insert.

The anode and its associated grid structure are coupled to the chamber envelope via a linear bellows drive enabling the drift distance to be varied. A stop attached to the guard ring farthest from the cathode is positioned such that at the maximum drift distance, the anode grid is coplanar with the center plane of this guard ring and is indicated by electrical continuity between the guard ring and anode grid. Thus, decreasing the drift distance in increments of 0.5 cm ensures that the anode grid is coplanar with each successive guard ring thereby minimizing distortions of the electric field. Increments in drift distance are accurately measured using a high-resolution (0.0002 cm/div.) micrometer indexed to the drive outside the

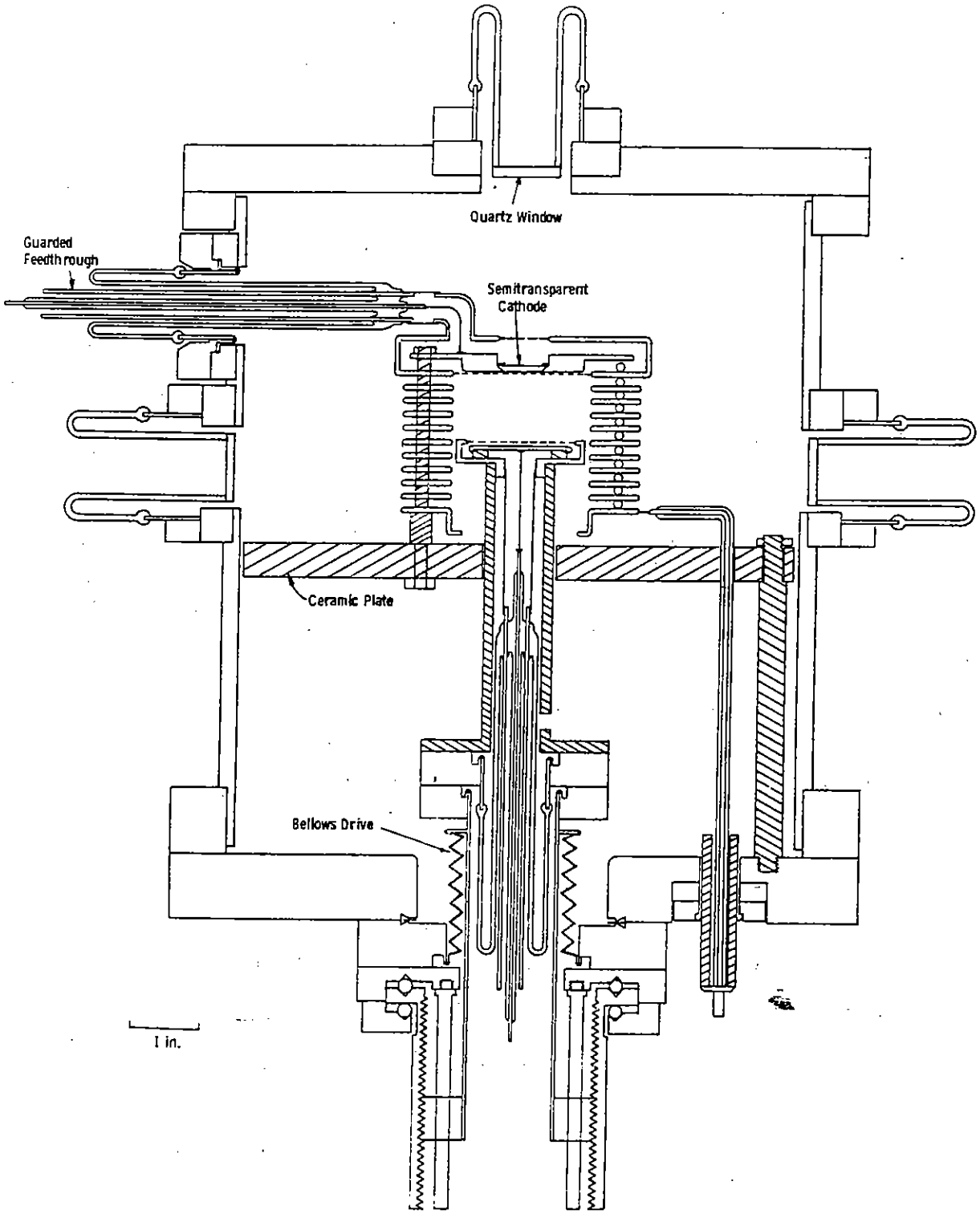

Figure 1. Sectional drawing of the drift tube.

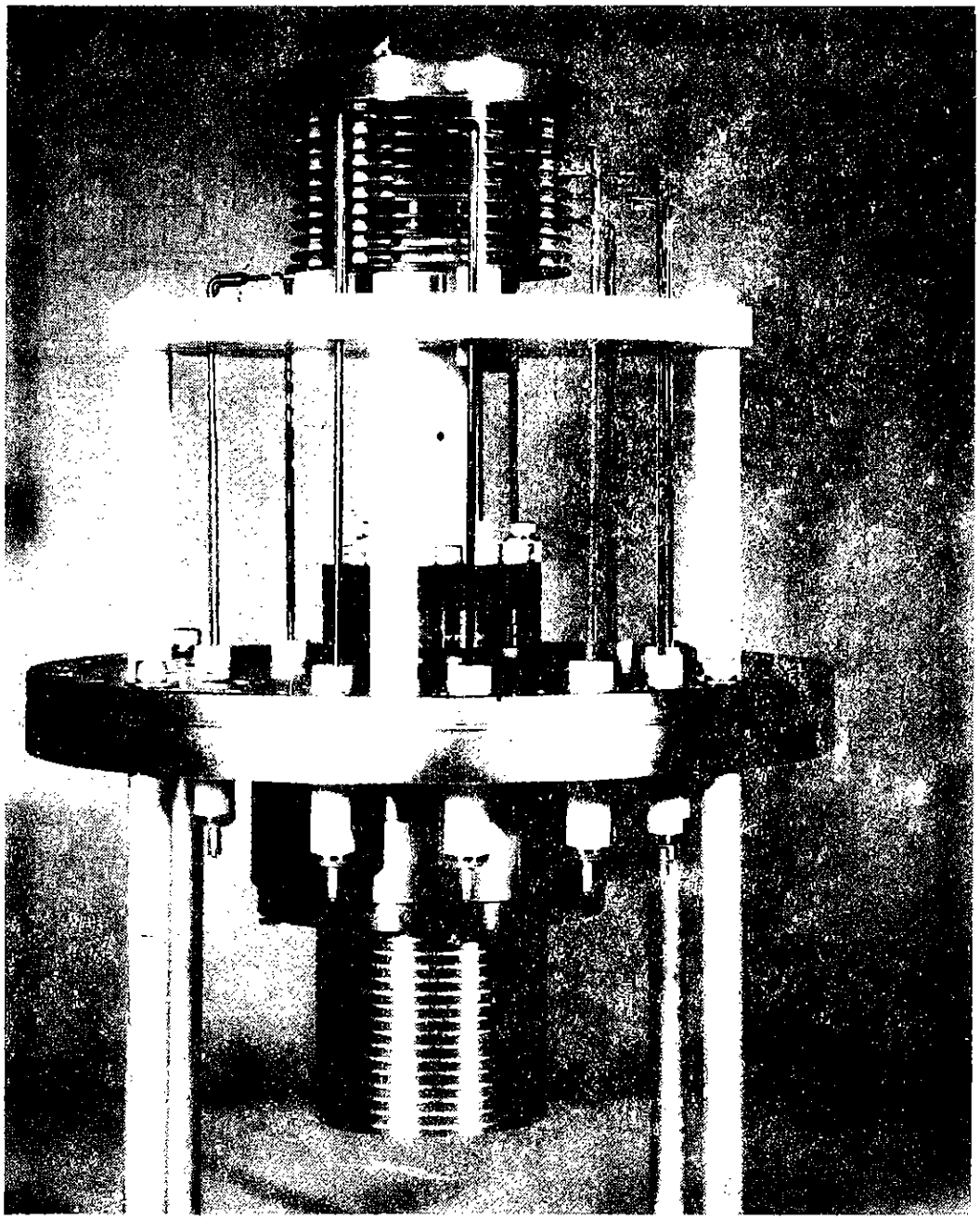

Figure 2. Photograph of the internal structure of the drift tube.

chamber envelope. In this way the total drift distance between anode and cathode may be varied from 0.7 cm to 5.2 cm.

The tube is designed so that either the cathode or anode may be connected to high potential. Connection to each guard ring is made by an insulated lead to a separate vacuum feedthrough in the chamber envelope.

The stainless steel chamber enclosing the drift tube also contains three quartz windows, one to provide optical access colinear with the axis of the drift tube and two for providing an optical path through the annular guard rings transverse to the axis of the drift tube.

2. VACUUM AND GAS HANDLING SYSTEM

The chamber is connected to an ultra high vacuum and gas handling system shown in Figure 3. Materials used for fabrication of the drift tube and its associated vacuum system have been chosen to be compatible with corrosive gases. All system components within the dashed rectangle in Figure 3 are baked during vacuum processing of the system prior to admission of gas to the chamber. Following a bakeout of the system at 350°C for 20 h, the residual pressure is reduced to the low 10^{-9}-torr (10^{-7}-Pa) range.

The gas pressure in the chamber is measured using a system of two differential Baratron (Ref. 2) gauges having a combined specified accuracy of ±0.1% over the range from 0.1 to 1000 torr. The reference side of each gauge may be separately evacuated to a pressure $< 10^{-6}$ torr using the ion pump. Alternately, the reference side of the 10-torr gauge (which is connected to the measurement side of the 1000-torr gauge) may be pressurized from the nitrogen supply. Thus, for pressures in the range 0.1 torr to 10 torr the pressure is measured directly using the 10-torr gauge with its reference side evacuated. For pressures greater than 10 torr, the 10-torr gauge is used as a null indicator (differential pressure $< 10^{-3}$ torr) by allowing nitrogen into its reference side and reading the pressure directly with the 1000-torr gauge. Comparisons of the two gauges over the limited pressure range where both gauges are within their specified accuracy limits show consistency to ±0.1%.

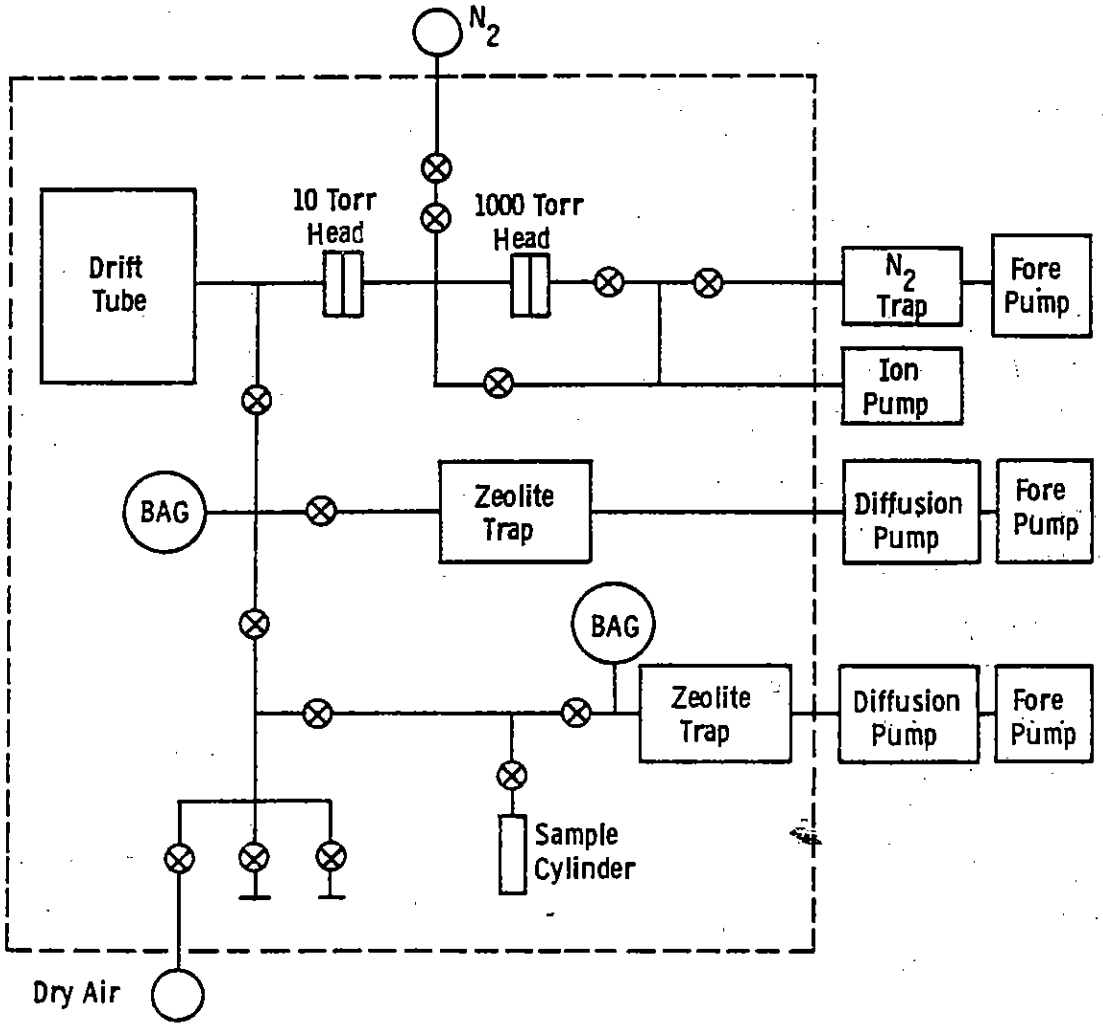

Figure 3. Schematic drawing of the vacuum and gas-handling system.

3. MEASUREMENT CIRCUITRY

The experimental arrangement used for the measurement of current waveforms from the drift tube is shown schematically in Figure 4 and is a modification of that used by Stelman et al. (Ref. 3). A chain of 0.1% precision resistors across a bipolar DC power supply is used to derive the potentials applied to the drift tube, and the potential difference between the cathode and anode is measured to better than ±0.1% using a digital voltmeter. A pulse of ultraviolet (UV) radiation from an externally mounted source illuminates the rear surface of the semi-transparent cathode via the quartz window in the chamber envelope. This provides the initial photoelectron pulse emitted to the drift region. The resulting arrival-time currents of electrons and negative ions at the anode or of positive ions at the cathode are detected when they pass through the grid immediately adjacent to each collecting electrode. The electrode current signal is amplified and fed to a waveform digitizer (Biomation Model 6500) and signal averager (Nicolet Model 1070) and eventually stored on 9-track tape (Kennedy Model 9700). Data are accumulated in the signal averager at a repetition rate ~ 30-100 s^{-1} until the signal/noise ratio has attained a satisfactory value. Typically this requires the summation of between 10^4 and 10^5 digitized current waveforms.

Although the signal averager is effective in improving the ratio of true signal to random noise, sources of nonrandom (systematic) noise and direct current (DC) drift are unaffected. Despite careful shielding nonrandom noise, particularly that associated with pick-up from the pulsed light source, remains significant. In order to remove this source of noise from the signal accumulated from many repetitions of the experiment it has been found necessary to arrange the transfer of data from the waveform digitizer to the signal averager so that alternate pulses are added to and subtracted from the data already stored in the signal averager. A synchronized shutter between the pulsed light source and the drift tube is arranged so that during the add cycle the light pulse from the UV source is transmitted into the drift tube, while during the subtract cycle the light pulse is blocked.

The logic circuitry required for operating the system in this mode is shown schematically in Figure 5 and the derived control signals and synchronized light pulses are shown in Figure 6. Encoder 1 signal occurs at the

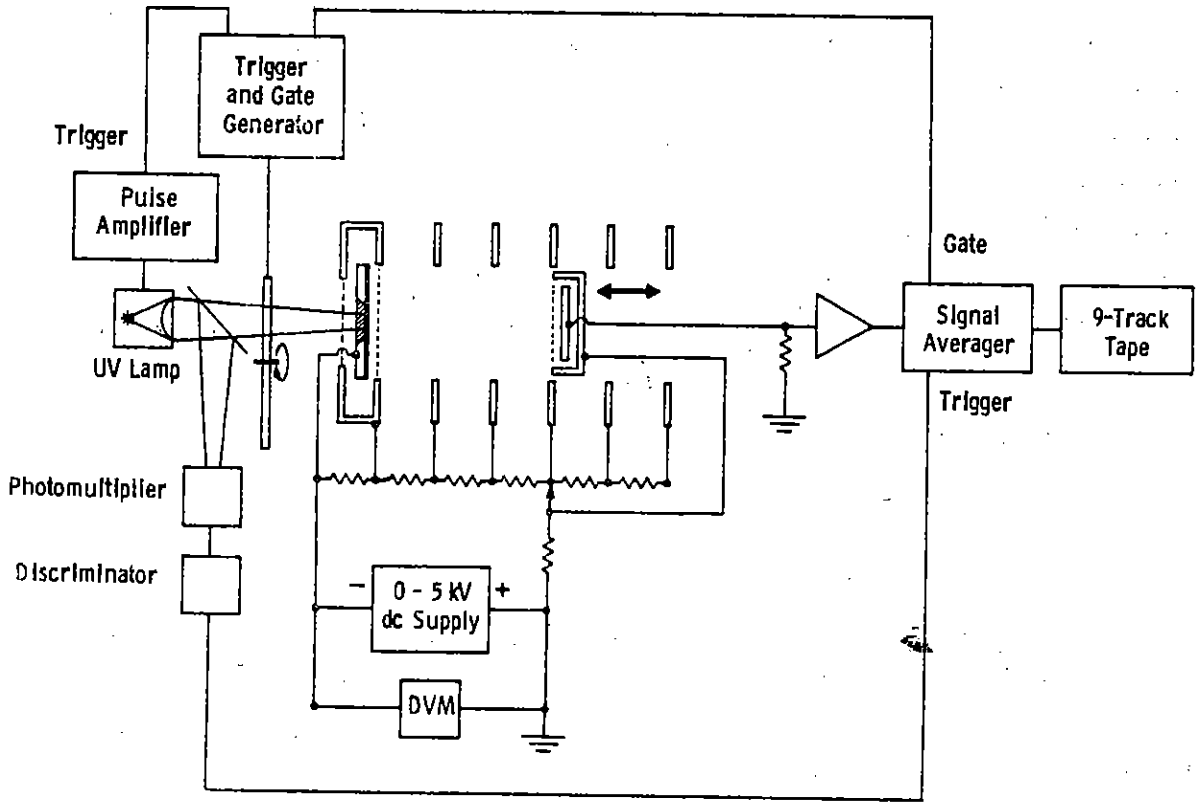

Figure 4. Experimental arrangement of the system for measuring current waveforms.

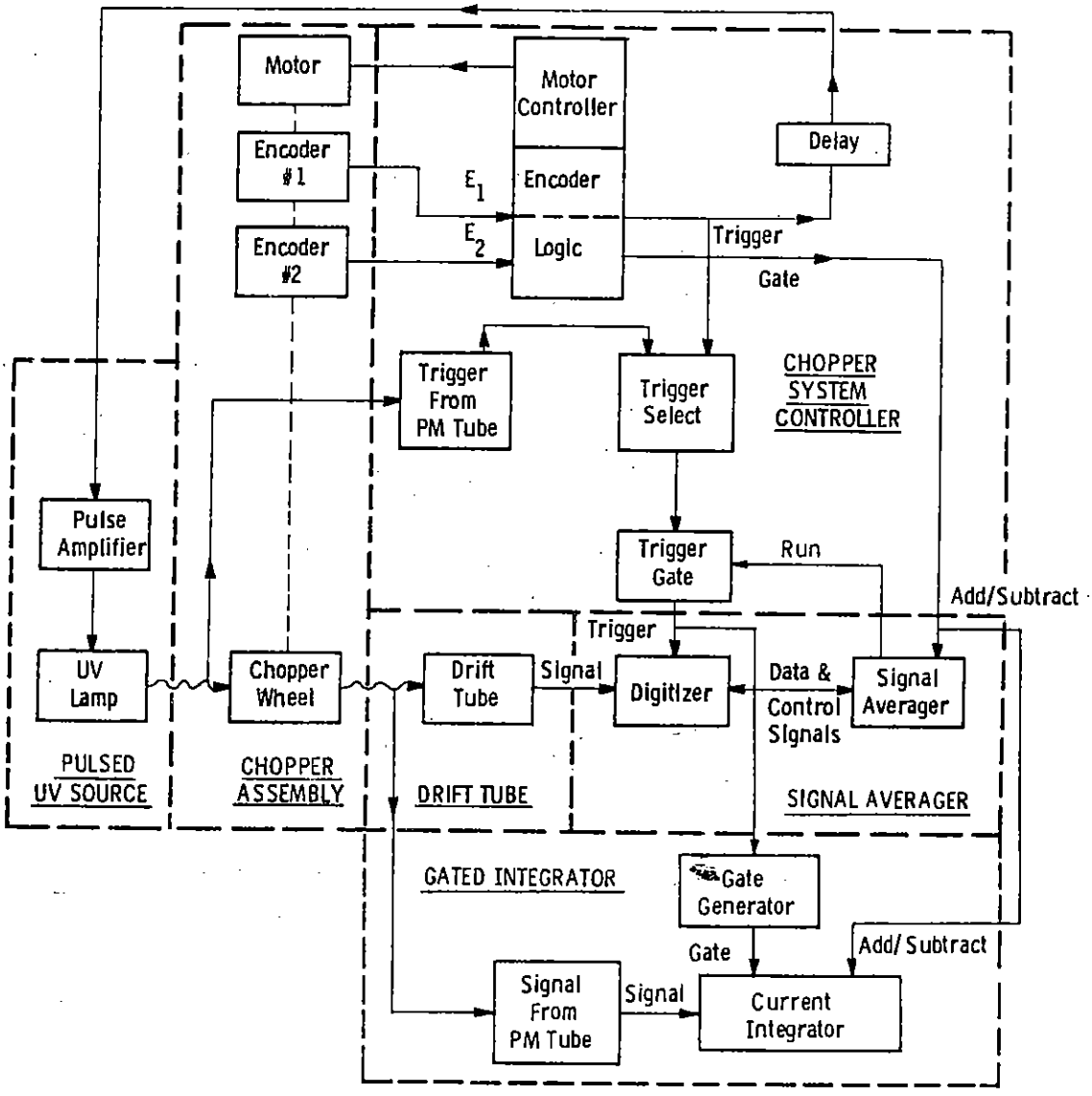

Figure 5. Schematic of the logic signals for operation of the pulsed drift tube.

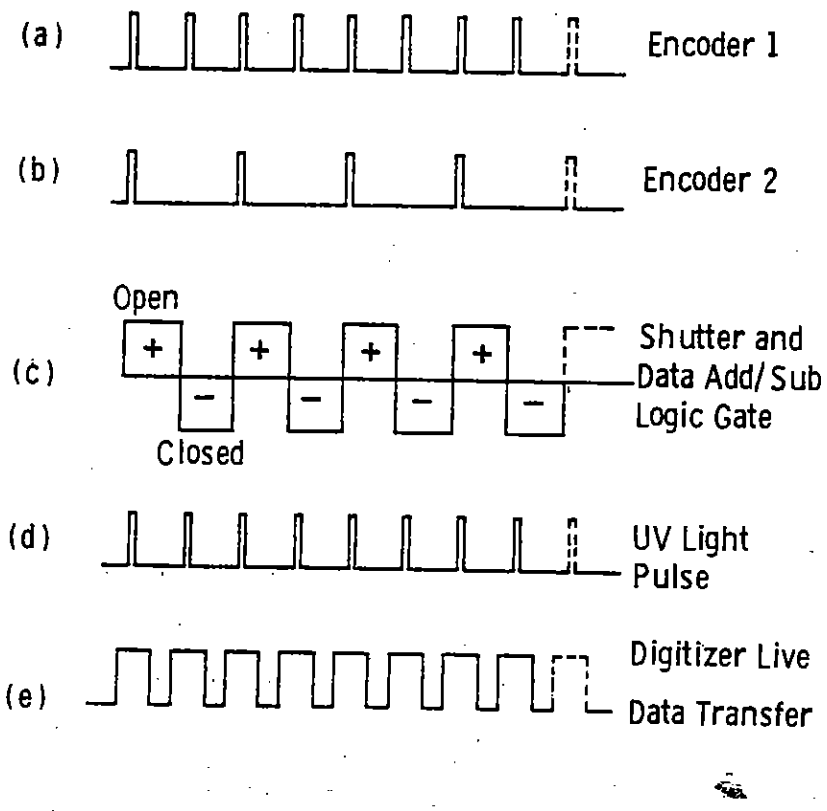

Figure 6. Data logic control signals and the synchronized light pulses.

start of every cycle (open and closed) of the chopper wheel while encoder 2 occurs only at the beginning of each open cycle of the wheel; these signals are shown on lines (a) and (b) of Figure 6. Line (c) represents both the state of the chopper wheel (open or closed) and the mode (add or subtract) of the signal averager. Line (d) represents the UV light pulse which is delayed from the encoder 1 pulses sufficiently to ensure that all logic levels are properly set. Line (e) represents the state of the digitizer and signal averager. When the level indicated is high, the digitizer is live and storing a received transient in digital form on a preset time scale. During this period the signal averager is quiescent. After the predetermined sweep time of the digitizer, the stored data (representing the just completed single sweep) are transferred to the signal averager. The data are added to or subtracted from the data previously stored in the memory of the signal averager depending on the state of the logic gate represented on line (d) of Figure 6.

The repetition frequency of the experiment is determined by the speed of rotation of the stepper motor. Each cycle must encompass both the sweep time of the digitizer (generally, in the range from 2 μs to 2 ms) and the time (10 ms) required to transfer the data from the digitizer to the signal averager. This limits the repetition frequency of the experiment to values less than 100 $s.^{-1}$ Data acquisition is initiated by the signal averager which latches the trigger gate open for the preset number of cycles. The trigger pulses are derived either from the encoder 1 pulses or from a photomultiplier which views a fraction of the UV light pulse. The latter is necessary when operating on the fastest time scales in order to minimize the jitter between the triggering of the digitizer and the release of the electron pulse from the photocathode of the drift tube. On the slower time scales it is necessary to trigger the digitizer in advance of the UV light pulse by an amount at least equivalent to one channel width of the electron component of the total waveform. Under these conditions the trigger pulses are derived from the encoder 1 pulses and the UV light source is triggered after an appropriate delay time.

This scheme removes from the accumulated signal all components of the background which occur repetitively in synchronism with the pulsed light source, including any DC component. In the present application it has also

been found necessary to ensure that the chopper wheel presents the same electrical screening profile in both the add/open position and subtract/blocked position. This is achieved using a metal wheel consisting of all open segments with alternate segments masked by nonconducting opaque material. During the course of the present investigation an improved version (Ref. 4) of this data collection scheme has been incorporated which also provides cancellation of quadratic and lower order terms of the time-dependent background. This has been found to yield improved signal/noise in the measured waveforms particularly when long averaging times are necessary.

Three different pulsed UV sources have been used during the course of the present investigation for liberating the initial photoelectron pulse from the cathode. For the measurements of electron drift velocity a spark discharge source (Xenon Corporation Model 437A Nanopulser with a Type N-789B Head) has been used operating in air with an input energy ~ 1 mJ/pulse. The UV output from this source has a risetime of 10 ns and a halfwidth of 20 ns and liberates ~ 10^5 photoelectrons/pulse from the cathode.

For measurements of ion mobility, attachment, and ionization two different sources have been used. The earlier measurements were carried out using a deuterium lamp pulsed at a peak current ~ 4 A. The rise and fall times of the radiation pulse are ~ 20 ns with a pulse width which may be varied over the range from 70 ns to 150 μs. For the longer pulse durations the photoelectron yield/pulse is comparable to the spark discharge source. Later measurements were carried out using a pulsed xenon lamp (EGG Type FX-265 UV) operated at input energies over the range from 10 mJ/pulse to 100 mJ/pulse. Over this range the risetime of the UV output varies from 65 ns to 185 ns and the halfwidth varies from 145 ns to 385 ns giving a cathode photoemission in the range from 10^6 to 2 x 10^7 electrons/pulse. The higher intensity from this source compared with the deuterium source results in a significant improvement in the signal/noise ratio of the measured ion waveforms.

The configuration shown in Figure 4 corresponds to that used for measuring electron and negative ion signals arriving at the anode. For measurements of positive ion signals arriving at the cathode, the measuring circuitry is transferred to the cathode and the ground of the DC supply is transferred to the negative side. The ability of the present system to resolve the

individual negative ion and positive ion components under conditions where attachment and ionization are occurring simultaneously simplifies the determination of the attachment and ionization coefficients as discussed in Section II.4. For these measurements, normalization of the positive ion and negative ion signals to the initial photoelectron current is necessary. This is accomplished by monitoring the UV radiation entering the drift tube. A fraction of the UV output from the lamp is diverted by a suprasil quartz beamsplitter, placed between the chopper wheel and the drift tube, onto a photomultiplier as shown schematically in Figure 5. The output from the photomultiplier is fed to a gated current integrator whose gate width is adjusted to be slightly longer than the UV pulse duration. The input to the integrator is arranged to be active for the same number of preset cycles for which the signal averager is accumulating current waveforms. Preliminary measurements were carried out to verify the correspondence between the UV signal and the total charge collected from the drift tube. These showed proportionality to within 1% justifying the normalization procedure adopted.

4. DETERMINATION OF SWARM PARAMETERS

a. Electron Waveforms

Under conditions where the duration (δt) of the initial electron pulse leaving the cathode is such that $\delta t \ll d/w_e$, where d is the total drift distance and w_e is the electron drift velocity, solution of the continuity equation for electrons leads to the following expression (Refs. 5 and 6) for the time-dependent electron current [$I_e(d,t)$] arriving at the anode:

$$I_e(d,t) = [Q_o w_e/(4\pi D_L t)^{1/2}] \exp[-(d - w_e t)^2/4D_L t + (\alpha - \eta)w_e t] \qquad (2)$$

In Equation (2), Q_o is the initial net electron charge released from the cathode, D_L is the longitudinal diffusion coefficient, α is the ionization coefficient and η is the attachment coefficient. From Equation (2) the time τ_e corresponding to the arrival time at the anode of the peak of the electron current pulse is given to first order by

$$\tau_e \simeq (d/w_e)\,[1 - D_L/w_e d + 2D_L\,(\alpha - \eta)/w_e] \qquad (3)$$

By making measurements of τ_e as a function of d, errors due to the finite width of the pulse, end effects, and (to first order) diffusion effects are eliminated. However, effects due to attachment and ionization are not removed since, from Equation (3), the slope of the linear plot of τ_e versus d is given by $[1 + 2D_L (\alpha - \eta)/w_e]/w_e$, in contrast to the value $1/w_e$ obtained in the absence of ionization or attachment. Thus, the true value of w_e is less than d/τ_e if $\eta > \alpha$ and larger than d/τ_e if $\alpha > \eta$. Usually, experimental conditions are chosen so that $D_L \phi\alpha - \eta\phi/w_e \ll 1$ making the correction to w_e negligibly small.

The electron reduced mobility μ_e is readily determined from the drift velocity through the relation

$$\mu_e = w_e/(E/N)\ N_o \tag{4}$$

where N_o ($= 2.688 \times 10^{25} m^{-3}$) is the gas number density corresponding to 760 torr at 273K.

In general, seven different drift distances have been used for the determination of w_e at each value of E/N. A typical example of the raw data is shown in Figure 7, corresponding to data taken at a value of $E/N = 1.000 \times 10^{-20}$ V·m^2 and a gas density $N = 1.077 \times 10^{24}$ m^{-3}. The part (a) of Figure 7 is an analog presentation of the stored digital data corresponding to seven superimposed electron waveforms taken at drift distances ranging from 2.2 to 5.2 cm in increments of 0.5 cm. The lower part of the photograph shows the magnified peaks at drift distances of 2.2 and 5.2 cm to indicate the resolution attained in the measurements. The part (b) of Figure 7 shows a plot of the arrival time τ_e' of the peak of the waveform as a function of drift distance, these data being obtained from the stored digital values corresponding to the waveforms shown in the photograph. In all cases the plots are found to be linear and the values of w_e are obtained directly from the slope of the linear regression fit to each plot. Since the drift velocity is obtained from differential measurements, no effort has been made to determine absolutely the time t=0 at which the initial electron pulse is released from the cathode. Thus, as illustrated in Figure 7(b), the plot of τ_e' versus d does not necessarily pass through the origin.

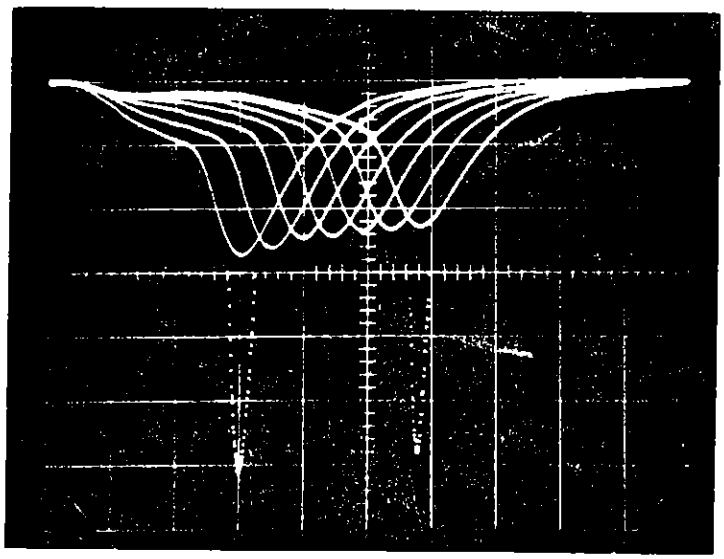

(a) Analog presentation of stored digital data corresponding to seven superimposed electron waveforms taken at drift distances ranging from 2.2 to 5.2 cm in increments of 0.5 cm. The lower part of the photograph shows the peaks at 2.2 and 5.2 cm magnified to indicate the resolution attained. The time scale is 5 ns/point (∿ 0.5 μs/division).

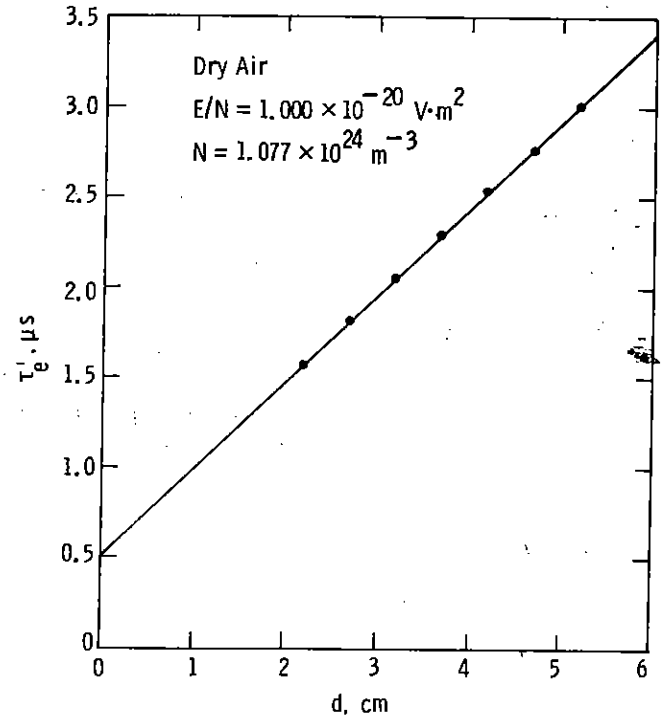

(b) Plot of τ'_e versus d derived from the data shown in the photograph. The line represents a linear regression fit to the experimental points. E/N = 1.000 x 10^{-20} V·m^2, N = 1.077 x 10^{24} m^{-3}.

Figure 7. Sample of the raw data used for the determination of electron drift velocity.

b. Ion Waveforms

Under conditions where the duration (δt) of the initial electron pulse is such that $\delta t \ll d/w_{\pm}$ (where w_+ and w_- are the drift velocities of positive ions and negative ions, respectively) solution of the continuity equation for negative ions leads to the following expression (Ref. 7) for the time-dependent negative ion current [$I_-(d,t)$] arriving at the anode:

$$I_-(d,t) = Q_o \eta w_- \exp[(\alpha - \eta)(d - w_- t)] \quad \text{for } 0 \leq t \leq d/w_-$$

$$I_-(d,t) = 0 \quad \text{for } t > d/w_- \tag{5}$$

Similarly, the time-dependent positive ion current $I_+(0,t)$ arriving at the cathode is given by

$$I_+(0,t) = Q_o \alpha w_+ \exp[(\alpha - \eta) w_+ t] \quad \text{for } 0 \leq t \leq d/w_+$$

$$I_+(0,t) = 0 \quad \text{for } t > d/w_+ \tag{6}$$

The positive and negative ion transit times, τ_+ and τ_-, respectively, are readily determined from the ion current waveforms as described above for the case of electrons. Examples of total current waveforms collected at the anode are given in Figure 8. Here, four superimposed waveforms are shown taken at a drift distance of 5.2 cm and a gas density of 3.235×10^{24} m^{-3} for values of E/N = 2.000, 3.000, 4.00, and 5.00×10^{-21} $V \cdot m^2$. For each waveform the first peak represents the collected current due to electrons which have crossed the drift space without suffering attaching collisions and the second peak is due to the collected current of negative ions formed in the drift region. Similar measurements of the total collected current at the cathode enable the positive ion component to be recorded at values of E/N where $\alpha > 0$. Thus, from measurements taken as a function of drift distance at constant E/N the values of w_+ and w_- are given from the slopes of the linear plots of τ_+ versus d, and t_- versus d, respectively. The ion reduced mobilities μ_+ and μ_- are defined by the relations

$$\mu_+ = w_+/(E/N)N_o; \quad \mu_- = w_-/(E/N)N_o \tag{7}$$

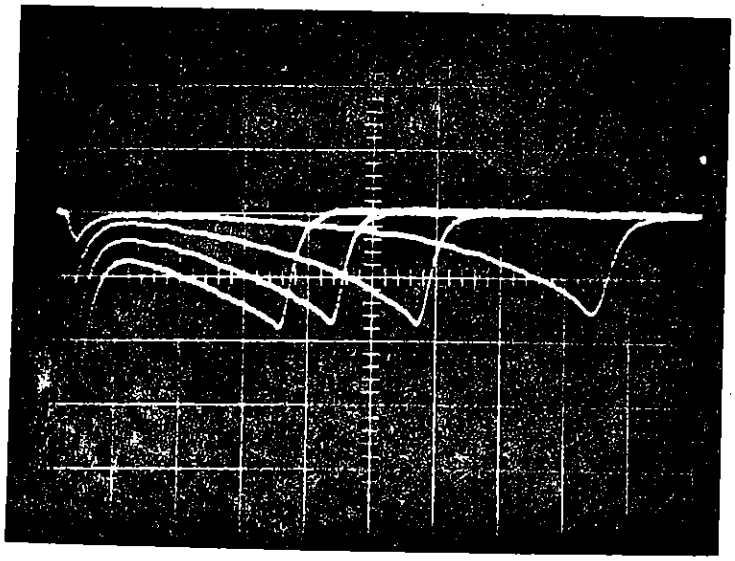

Figure 8. Sample of the raw measurements of negative ion waveforms. The photograph shows an analog presentation of stored digital data corresponding to four superimposed waveforms taken at values of E/N = 2.000, 3.000, 4.00, and 5.00 x 10^{-21} $V \cdot m^2$, $N = 3.235 \times 10^{24}$ m^{-3}, d = 5.2 cm. The time scale is 10 μs/point (∿ 1 ms/division).

The net ionization coefficient $(\alpha - \eta)$ may be determined from either the positive ion or negative ion waveforms. In practice, greater precision is obtained if the positive ion waveform is used when $\alpha > \eta$, and the negative ion waveform is used when $\eta > \alpha$.

Under conditions where only a single ion species is present, plots of $\ell n\ I_-(d,t)$ versus t or $\ell n\ I_+(0,t)$ versus t are linear and from Equations (5) and (6), have slopes $(\alpha - \eta)w_-$ and $(\alpha - \eta)w_+$, respectively. Thus, knowing w_- and w_+, $(\alpha - \eta)$ is determined. For situations where more than one ion species is present, the ion current waveforms are no longer purely exponential and $(\alpha - \eta)$ is more conveniently determined from the integrals of the current waveforms, i.e., from the charge collected. In the analysis of the charge waveforms, account must be taken of the different transmissions of the grids for electrons and ions.

Thus, at the anode, the charge of electrons Q_e^A, negative ions Q_-^A and total charge Q_T^A collected are given by

$$Q_e^A = f_1^2\ Q_o\ \exp(\alpha - \eta)d \tag{8}$$

$$Q_-^A = [f_1 f_2\ Q_o\ \eta/(\alpha - \eta)]\ [\exp(\alpha - \eta)d - 1] \tag{9}$$

$$Q_T^A = Q_o\ [\{[f_1 f_2\ \eta/(\alpha - \eta)] + f_1^2\}\ \exp(\alpha - \eta)d - f_1 f_2\ \eta/(\alpha - \eta)] \tag{10}$$

where f_1 and f_2 are the fractions of electrons and ions, respectively, transmitted by each grid. Writing $y^A = Q_T^A/Q_e^A$, it follows from Equations (8) and (10) that

$$y_{d\ +\ \Delta d}^A = y_d^A\ \exp{-(\alpha - \eta)\Delta d} + \{1 + (f_2/f_1)[\eta/(\alpha - \eta)]\}[1 - \exp{-(\alpha - \eta)\Delta d}] \tag{11}$$

where y_d^A and $y_{d+\Delta d}^A$ are the charge ratios at the drift distances d and $d + \Delta d$, respectively. Thus, by making measurements of the charge ratio Q_T^A/Q_e^A at a sequence of drift distances differing by a constant increment Δd, keeping E/N constant, the net ionization coefficient $(\alpha - \eta)$ is determined from the slope $\exp - (\alpha - \eta)\Delta d$ of the linear plot of $y_{d+\Delta d}^A$ versus y_d^A.

Similarly, at the cathode, the total charge Q_T^C collected is comprised of the initial electron charge leaving Q_e^C and the returning positive ion charge Q_+^C. The resulting expressions for Q_e^C, Q_+^C and Q_T^C are given by

$$Q_e^C = Q_o \tag{12}$$

$$Q_+^C = [f_1 f_2 \, Q_o \, \alpha/(\alpha - \eta)] \, [\exp(\alpha - \eta)d - 1] \tag{13}$$

$$Q_T^C = Q_o \, \{[f_1 f_2 \, \alpha/(\alpha - \eta)] \exp(\alpha - \eta)d - f_1 f_2 \, \eta/(\alpha - \eta)\} \tag{14}$$

leading to the corresponding expression for the charge ratio $y_d^C = Q_T^C/Q_e^C$ given by

$$y_{d+\Delta d}^C = y_d^C \exp(\alpha - \eta)\Delta d + [1 - f_1 f_2 \, \alpha/(\alpha - \eta)] \, [1 - \exp(\alpha - \eta)\Delta d] \tag{15}$$

The net ionization coefficient $(\alpha - \eta)$ is then determined from the slope $\exp(\alpha - \eta)\Delta d$ of the linear plot of $y_{d+\Delta d}^C$ versus y_d^C.

The ratio α/η is determined directly from the ratio of $(Q_+^C/Q_o)/(Q_-^A/Q_o)$ where normalization of the charge Q_+^C and Q_-^A collected at the cathode and anode is made to the charge Q_o (or more correctly to a charge proportional to Q_o) as discussed in Section II.3. Thus, knowing $(\alpha - \eta)$ and α/η, the individual coefficients α and η are determined.

For given values of E/N and Q_o, it is noted that the total charge Q_T^C collected at the cathode is larger than that collected at the anode Q_T^A by an amount $(f_1 f_2 - f_1^2) \exp(\alpha - \eta)d$. For perfectly transmitting grids, i.e., for $f_1 = f_2 = 1$, the expressions given by Equations (10) and (14) both reduce to the well-known form describing spatial current growth between planar electrodes under steady-state conditions.

At the limiting value of E/N, at which $\alpha = \eta$, Equations (5) and (6) show that $I_-(d,t)$ and $I_+(0,t)$ are constant for $t \leq d/w_-$ and $t \leq d/w_+$, respectively, and from Equations (9) and (13), $Q_-^A = Q_+^C = f_1 f_2 \, Q_o \eta d$. Thus, the limiting

value of E/N may be determined precisely from measurements of the ion component of the total current waveforms.

For values of E/N below the onset of ionization, $\alpha = 0$ and Equation (5) reduces to

$$I_-(d,t) = Q_o\, \eta\, w_-\, \exp[-\eta(d - w_- t)] \quad \text{for } 0 \leq t \leq d/w_-$$

$$I_-(d,t) = 0 \quad \text{for } t > d/w_- \tag{16}$$

Under conditions where only a single negative ion species is present, the attachment coefficient is determined from the slope ηw_- of a plot of $\ell n\, I_-(d,t)$ versus t, and the determined value of w_-. Such is the case for the waveforms shown in Figure 8. One of these taken at $E/N = 3.000 \times 10^{-21}$ V·m^2 is replotted in Figure 9 in semilog form (inverted for convenience) using the stored digital data. For the sake of clarity, every fifth point only has been plotted. The slope ηw_- is determined from a regression fit to the experimental points on the rising portion of the ion current waveform. Such a fit is shown by the straight line drawn in Figure 9. Precautions are taken during the measurement of the waveforms to ensure that the time constant of the measuring circuit $RC \ll 1/\eta w_-$. Thus, the ionic component of the waveform is undistorted by instrumental effects.

If more than one negative ion species is present, the attachment coefficient is determined from the charge waveform and Equation (11) reduces to

$$y^A_{d+\Delta d} = y^A_d \exp \eta\Delta d - \{1 - (f_2/f_1)\} \quad (\exp \eta\Delta d - 1) \tag{17}$$

Thus, η is determined from the slope $\exp \eta\Delta d$ of a plot of $y^A_{d+\Delta d}$ versus y^A_d.

The above analysis demonstrates clearly that differential measurements are mandatory if meaningful values (free from grid transmission effects) of both $(\alpha - \eta)$ and η are to be obtained from charge waveforms derived from a drift tube of this type. As pointed out previously, the charge waveforms are the most convenient data to use when more than one ion species is present. Neglect of grid transmission effects not only leads to incorrect values of the coefficients but also to an incorrect functional dependence of the

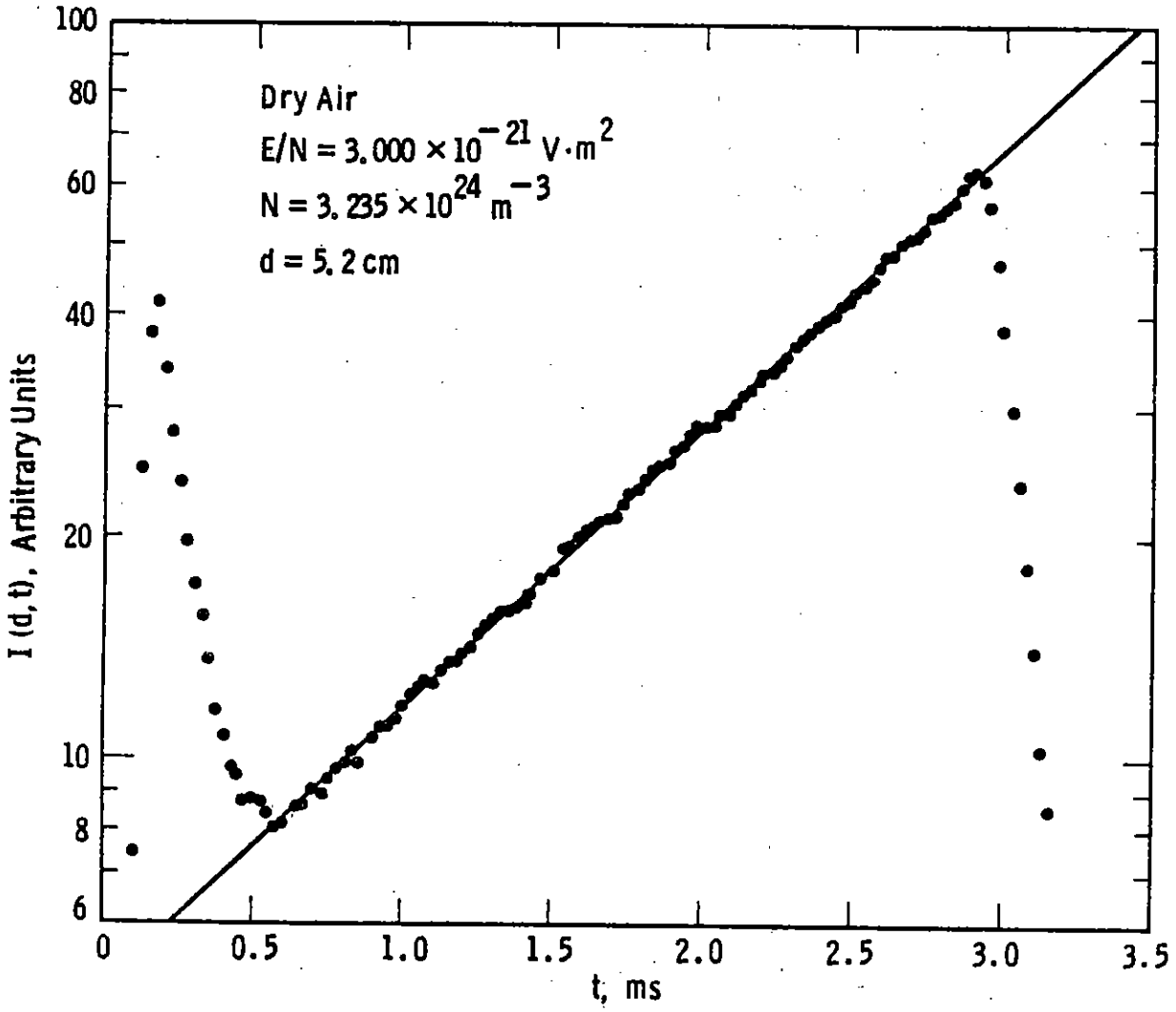

Figure 9. Semilog plot of $I_-(d,t)$ versus t obtained using the stored digital data corresponding to one of the waveforms shown in Figure 8. The straight line is a regression fit to the experimental points on the rising portion of the negative-ion signal. $E/N = 3.000 \times 10^{-21}$ V·m^2, $N = 3.235 \times 10^{24}$ m^{-3}, d = 5.2 cm.

coefficients on E/N since the value of f_2/f_1 is also a function of E/N. Present measurements taken at low E/N where only a single negative ion species is observed have shown that values of η determined from the current waveforms and from the charge waveforms agree to within the uncertainty of the measurements when proper account is taken of grid transmission effects. The determination of the parameters η, α and w_e, as functions of E/N enables the rate coefficients for attachment $k_a = \eta w_e/N$ (for a two-body process) or $k_a = \eta w_e/N^2$ (for a three-body process) and for ionization $k_i = \alpha w_e/N$ to be determined as functions of E/N.

III. RESULTS

The present measurements have been carried out in dry air with the CO_2 removed. The gas was supplied by Matheson Co. together with the analysis of the composition given in Table 1.

1. ELECTRON MOBILITY

The electron drift velocity is determined from the slope of the arrival time of the peak of the electron component of the anode current as a function of drift distance. For every plot analyzed, the experimental points differ from a linear regression fit to the data by less than 1% and in most cases by less than 0.5%.

A summary of the values of w_e and the derived reduced mobility μ_e as a function of E/N is given in Figure 10 and in Table 2. The upper abscissa scales in Figure 10 (along with most of the subsequent figures) show the corresponding values of electric field at atmospheric density for three different altitudes, 0 km, 15 km, and 30 km. The data cover the range of E/N from 6×10^{-22} to 3×10^{-19} V·m^2. The uncertainty in the values of w_e and μ_e is estimated to be ± 1% for values of E/N ≤ 10^{-19} V·m^2 and ± 2% for values of E/N > 10^{-19} V·m^2. No corrections have been applied to the data for attachment or ionization effects. Based on available knowledge of the parameters α, η, and D_L/μ_e, such corrections are estimated to be less than 0.5% (i.e., less than the assigned uncertainty) for values of E/N ≤ 2×10^{-19} V·m^2. For values of E/N > 2×10^{-19} V·m^2, the correction due to ionization increases monotonically with increasing E/N and may be as much as 2% at a value of E/N = 3×10^{-19} V·m^2.

A comparison of the present values of electron mobility with previous data (Refs. 8-14) is presented in Figure 11. For the sake of clarity, the present data are denoted by a smooth curve drawn through the experimental points shown in Figure 10. The left ordinate scale represents the value of reduced mobility μ_e while the right ordinate corresponds to the mobility at a density $N_o = 2.688 \times 10^{25}$ m^{-3}. Also indicated in Figure 10 by the arrows on the left ordinate are the value of the mobility of thermal electrons, 1.61 m^2/V·s,

TABLE 1. COMPOSITION OF THE DRY AIR USED IN THE PRESENT MEASUREMENTS

Gas	Fractional Concentration (by volume)
Nitrogen	0.781
Oxygen	0.209
Argon	0.0097
Carbon Dioxide	4.4×10^{-6}
Carbon Monoxide	$< 4 \times 10^{-6}$
Total Hydrocarbons	$< 4 \times 10^{-6}$
Water	11×10^{-6}

TABLE 2. VALUES OF THE ELECTRON MOBILITY IN DRY AIR.

E/N 10^{-21} V·m^2	EN_o/N 10^4 V/m	$\mu_e N$ 10^{24}/V·m·s	$\mu_e N/N_o$ m^2/V·s
0.600	1.613	8.25	0.307
0.700	1.882	7.59	0.282
0.800	2.150	7.10	0.264
0.900	2.419	6.78	0.252
1.000	2.688	6.58	0.245
1.250	3.360	6.04	0.225
1.500	4.03	5.39	0.201
1.750	4.70	5.09	0.189
2.000	5.38	4.77	0.177
2.500	6.72	4.16	0.155
3.000	8.06	3.73	0.139
3.500	9.41	3.40	0.127
4.00	10.75	3.18	0.118
4.50	12.10	2.96	0.110
5.00	13.44	2.82	0.105
6.00	16.13	2.58	0.0961
7.00	18.82	2.39	0.0887
8.00	21.50	2.24	0.0832
9.00	24.19	2.12	0.0789
10.00	26.88	2.09	0.0777
12.50	33.60	1.94	0.0723
15.00	40.3	1.80	0.0670
17.50	47.0	1.71	0.0638
20.00	53.8	1.64	0.0610
25.00	67.2	1.56	0.0582
30.00	80.6	1.49	0.0556
35.00	94.1	1.43	0.0530
40.0	107.5	1.40	0.0519
45.0	121.0	1.36	0.0504
50.0	134.4	1.33	0.0496
60.0	161.3	1.24	0.0461
70.0	188.2	1.21	0.0449
80.0	215.0	1.20	0.0446
90.0	241.9	1.21	0.0451
100.0	268.8	1.21	0.0450
125.0	336.0	1.17	0.0434
150.0	403	1.12	0.0417
175.0	470	1.12	0.0417
200.0	538	1.10	0.0407
250.0	672	1.01	0.0375
300.0	806	0.98	0.0366

$N_o = 2.688 \times 10^{25}$ m^{-3}

Estimated uncertainties in the measured quantities are:

E/N: ± 0.2%

$\mu_e N$, $\mu_e N/N_o$: ± 1% for $E/N \leq 10^{-19}$ V·m^2; ± 2% for $E/N > 10^{-19}$ V·m^2

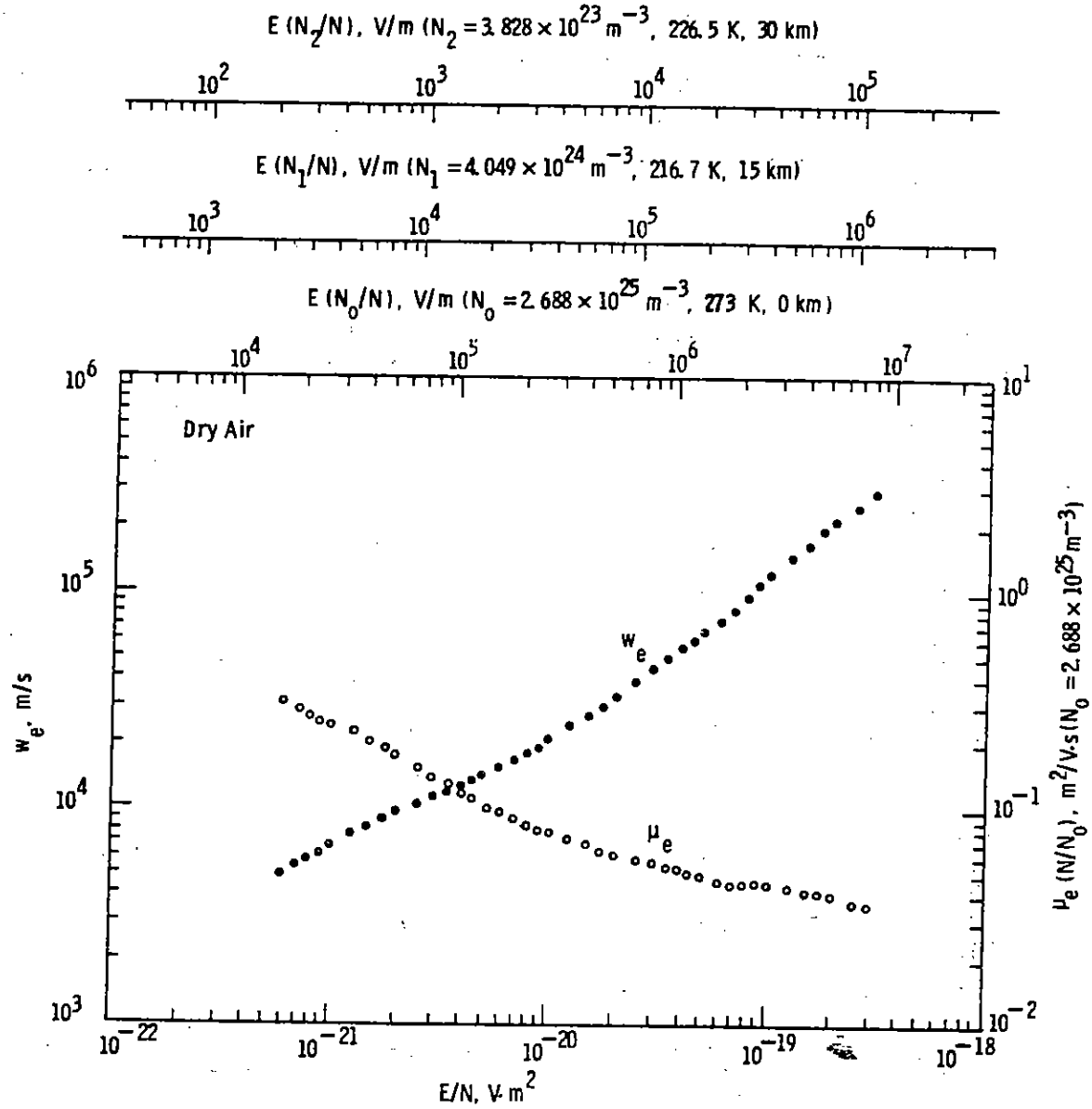

Figure 10. Summary of the present measurements of electron drift velocity or electron mobility as a function of E/N.

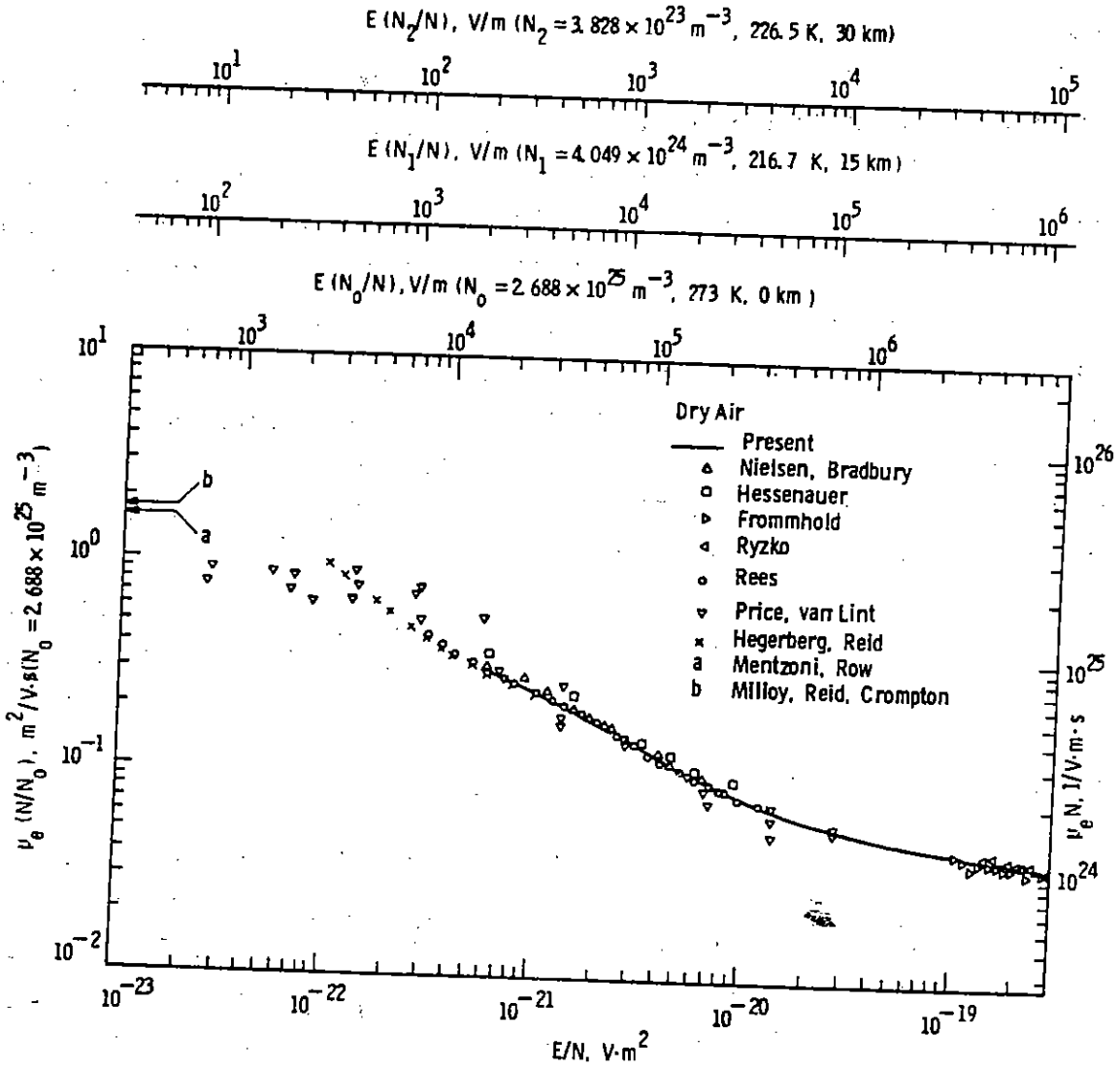

Figure 11. Comparison of the present measurements of electron mobility with previous data. The data of Price and van Lint correspond to the corrected values reported by Pettus and Crevier. The arrows on the ordinate correspond to determinations of the mobility of thermal electrons.

deduced from the measurements of electron collision frequencies in oxygen (Ref. 15) and nitrogen (Ref. 16), and the value of 1.75 $m^2/V \cdot s$ deduced from measurements of electron mobility in dry air-carbon dioxide mixtures (Ref. 17).

As may be seen from Figure 10, the data obtained in the present study are the first comprehensive set of measurements in the range of E/N from 10^{-20} to 10^{-19} $V \cdot m^2$. In the region of overlap, the present data are in excellent agreement (to within the combined uncertainty limits which range from ± 2% to ± 5%) with the measurements of Rees (Ref. 12) and of Hegerberg and Reid (Ref. 14). The values of Nielsen and Bradbury (Ref. 8) and of Hessenauer (Ref. 9) are up to 10% and 20% larger, respectively, than the present results.

It is interesting to note that the data of Hegerberg and Reid (Ref. 14) indicate that the electron mean energy is still above thermal at a value of $E/N = 10^{-22}$ $V \cdot m^2$. This is in contrast to the measurements of Price and van Lint (Ref. 13) which exhibit an approximately constant mobility over the range of E/N from ~ 2.5×10^{-23} to ~ 3×10^{-22} $V \cdot m^2$. A possible explanation for this discrepancy may be that sufficient amounts of water vapor were present in the experiments of Price and van Lint to cause thermalization of electrons to higher values of E/N by virtue of the large inelastic cross section of electrons in water vapor.

2. ION MOBILITIES

The ion mobility is determined from the slope of the measured time of the peak of the arrival spectrum of negative ions at the anode, or positive ions at the cathode, as a function of drift distance. As in the case of electrons, seven different drift distances have been used for the determination of w_- or w_+ at each value of E/N. In all cases, plots of τ_- or τ_+ as a function of drift distance are found to be linear and the values of w_- or w_+ are obtained directly from a linear regression fit to each plot. In every case, the experimental points differ from the linear regression fit by less than ± 0.5%. No corrections to the values are required, since errors due to the finite width of the initial photoelectron pulse, end effects, and (to first order) diffusion effects are eliminated by making differential measurements. The uncertainty in the measurements of ion mobility is estimated to be ± 1%.

A summary of the values of reduced negative-ion mobility are given in Table 3 and Figure 12. The negative-ion waveforms show the presence of only one dominant species. However, based on the widely different mobilities, the identity of the ions for values of $E/N \leq 4 \times 10^{-20}$ V·m^2 is probably different from that for $E/N \geq 6 \times 10^{-20}$ V·m^2 and the dashed line in Table 2 indicates this distinction.

At low values of E/N, previous work (Ref. 18) in pure oxygen and oxygen-nitrogen mixtures has shown that the primary ion is O_2^- formed in the three-body reaction

$$e + O_2 + M \rightarrow O_2^- + M \tag{18}$$

where the third body M is either an oxygen or nitrogen molecule. Among the possible reactions of the O_2^- ions which can occur are

$$O_2^- + O_2 + O_2 \rightarrow O_4^- + O_2 \tag{19}$$

$$O_2^- + O_2 + CO_2 \rightarrow CO_4^- + O_2 \tag{20}$$

$$O_4^- + CO_2 \rightarrow CO_4^- + O_2 \tag{21}$$

with corresponding thermal rate coefficients of 3.0×10^{-43} m^6/s, 4.7×10^{-41} m^6/s, and 4.3×10^{-16} m^3/s, respectively (Refs. 19-21). Based on these rates and the densities of O_2 ($> 6 \times 10^{23}$ m^{-3}) and CO_2 ($< 3 \times 10^{18}$ m^{-3}) in the air mixtures used in the measurements for $E/N \leq 4 \times 10^{-20}$ V·m^2 the observed ion species is expected to be O_4^-. The values found for the mobility over the range from 6×10^{-22} to 4×10^{-20} V·m^2 are constant within the experimental uncertainty, having a mean value of 2.27×10^{-4} m^2/V·s. This suggests that, over this range of E/N, the observed ions are in thermal equilibrium with the gas. The only previous value of low-field mobility of O_4^- available for comparison is the value 2.30×10^{-4} m^2/V·s found (Ref. 22) for the low-field mobility of O_4^- in pure oxygen. It is noted that for naturally occurring abundancies of CO_2 in air (~ 0.03%) the final ion identity is expected to be CO_4^- formed predominantly via reactions of Equations (19) and (21). The value

TABLE 3. VALUES OF THE NEGATIVE-ION MOBILITY IN DRY AIR

E/N 10^{-21} V·m^2	EN_o/N 10^4 V/m	$\mu_- N$ 10^{21}/V·m·s	$\mu_- N/N_o$ 10^{-4} m^2/V·s
0.600	1.613	6.13	2.28
0.800	2.150	6.11	2.27
1.000	2.688	6.12	2.28
1.500	4.03	6.09	2.27
2.000	5.38	6.12	2.28
3.000	8.06	6.09	2.27
4.00	10.75	6.11	2.27
5.00	13.44	6.09	2.26
6.00	16.13	6.11	2.27
7.00	18.82	6.12	2.28
8.00	21.50	6.14	2.28
9.00	24.19	6.13	2.28
10.00	26.88	6.13	2.28
12.50	33.60	6.10	2.27
15.00	40.3	6.10	2.27
17.50	47.0	6.10	2.27
20.00	53.8	6.13	2.28
25.00	67.2	6.10	2.27
30.00	80.6	6.13	2.28
35.00	94.1	6.10	2.27
40.00	107.5	6.10	2.27
60.0	161.3	8.14	3.03
70.0	188.2	8.47	3.15
80.0	215.0	8.66	3.22
90.0	241.9	8.84	3.29
112.5	302.4	8.79	3.27
125.0	336.0	8.55	3.18
137.5	369.6	8.23	3.06
150.0	403	8.00	2.98
175.0	470	7.66	2.85

$N_o = 2.688 \times 10^{25}$ m^{-3}

Estimated uncertainties in the measured quantities are:

E/N: $\pm$ 0.2%

$\mu_- N$, $\mu_- N/N_o$: $\pm$ 1%

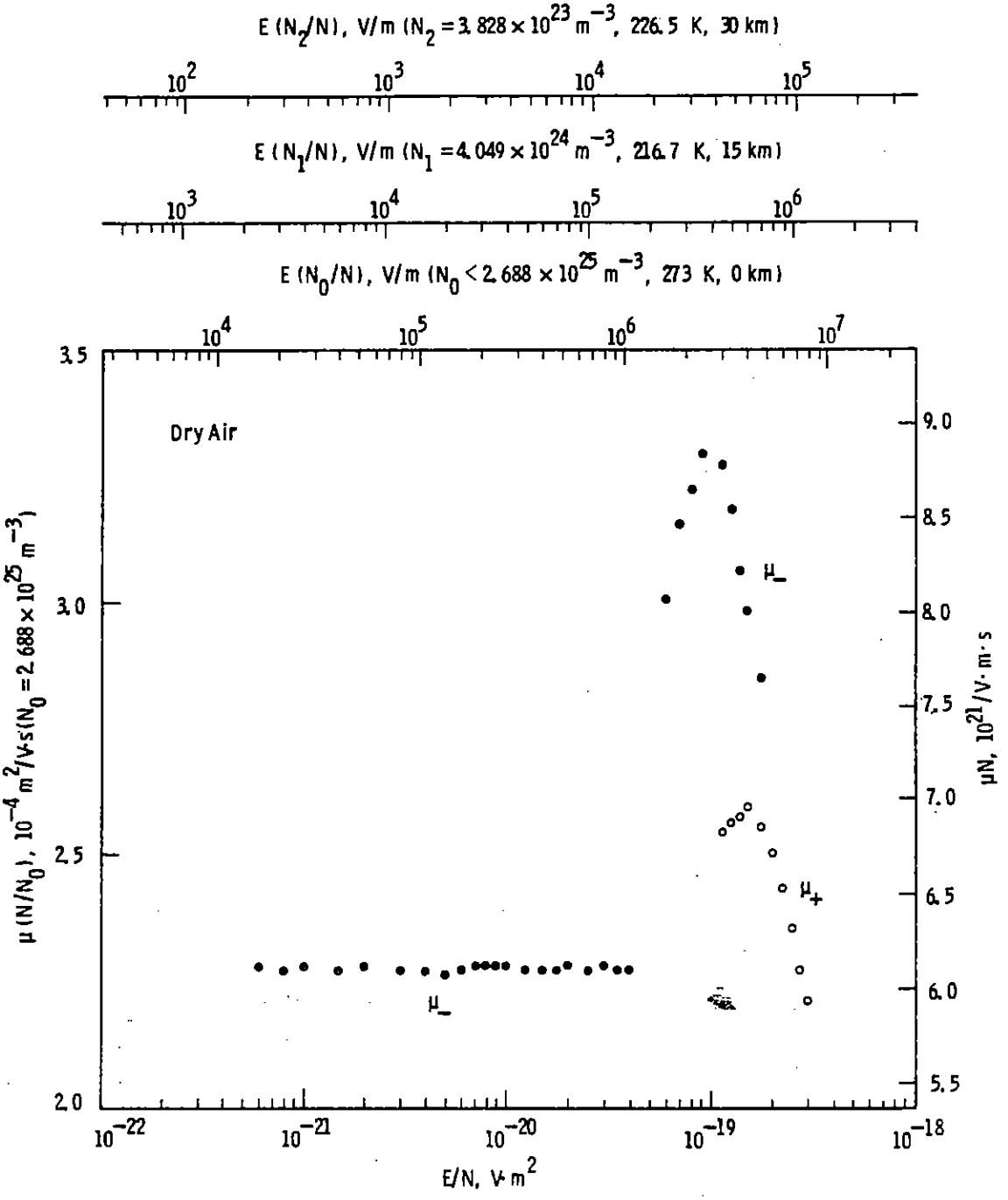

Figure 12. Summary of the present measurements of negative-ion (solid points) and positive-ion mobility (open points) as a function of E/N.

of the low-field mobility of CO_4^- ions in pure oxygen is only 3.5% larger than that of O_4^- ions in pure oxygen (Ref. 22).

At high values of E/N, the primary negative ion is expected (Ref. 18) to be O^- formed in the dissociative attachment reaction

$$e + O_2 \rightarrow O^- + O \tag{22}$$

Further reactions involving the O^- ions and their progeny are

$$O^- + O_2 + O_2 \rightarrow O_3^- + O_2 \tag{23}$$

$$O^- + O_2 + CO_2 \rightarrow CO_3^- + O_2 \tag{24}$$

$$O_3^- + CO_2 \rightarrow CO_3^- + O_2 \tag{25}$$

$$O^- + O_2 \rightarrow O_2^- + O \tag{26}$$

$$O^- + O_2 + H_2O \rightarrow O^-.H_2O + O_2 \tag{27}$$

$$O_3^- + O_2 + H_2O \rightarrow O_3^-.H_2O + O_2 \tag{28}$$

The first three reactions have thermal rate coefficients of 1.2×10^{-42} m^6/s, 3.1×10^{-40} m^6/s, and 5.5×10^{-16} m^3/s, respectively (Refs. 19, 20, and 23), while the fourth requires energetic O^- ions. The last two reactions have thermal rate coefficients of 1.3×10^{-40} m^6/s and 2.7×10^{-40} m^6/s, respectively (Ref. 20). Under the present experimental conditions the ions observed for values of $E/N > 6 \times 10^{-20}$ $V \cdot m^2$ are expected to be O_3^- ions. The varying mobility as a function of E/N indicates that the ions are non-thermal, as is to be expected (Ref. 22) at these values of E/N.

In the case of the positive ions, the waveforms observed do not exhibit a simple exponential dependence indicating the presence of more than one positive-ion species or the occurrence of ion conversion reactions. Thus, the values of positive-ion mobility summarized in Figure 12 and Table 4 refer to

TABLE 4. VALUES OF THE POSITIVE-ION MOBILITY IN DRY AIR

E/N 10^{-21} V·m^2	EN_o/N 10^4 V/m	μ_+N 10^{21}/V·m·s	μ_+N/N_o 10^{-4} m^2/V·s
112.5	302.4	6.83	2.54
125.0	336.0	6.88	2.56
137.5	369.6	6.91	2.57
150.0	403	6.95	2.59
175.0	470	6.85	2.55
200.0	538	6.73	2.50
225.0	605	6.54	2.43
250.0	672	6.33	2.35
275.0	739	6.11	2.27
300.0	806	5.94	2.21

$N_o = 2.688 \times 10^{25}$ m^{-3}

Estimated uncertainties in the measured quantities are:

E/N: $\pm$ 0.2%

μ_+N, μ_+N/N_o: $\pm$ 1%

the slowest ion, the only species clearly resolved in the present measurements.

The positive ions formed near the threshold for ion production by electron impact are expected to be N_2^+ and O_2^+ as a result of the reactions

$$e + N_2 \rightarrow N_2^+ + 2e \tag{29}$$

$$e + O_2 \rightarrow O_2^+ + 2e \tag{30}$$

Charge transfer reactions of the N_2^+ ions with either O_2 or CO_2 can lead to the formation of O_2^+ or CO_2^+ ions, respectively. In addition, the N_2^+ and O_2^+ ions can undergo three-body collisions with N_2 or O_2 forming N_4^+ or O_4^+ ions, respectively. At values of electron energy a few electron volts above the thresholds for N_2^+ and O_2^+ formation, N^+ and O^+ ions are formed by dissociative ionization. Further reactions of these ions with N_2, O_2 and CO_2 lead to the additional ion species NO^+, CO^+, CO_2^+, and O_2^+. Clearly, the positive-ion situation is more complex than that for the negative ions and it is difficult to draw any conclusions regarding the identity of the positive-ion species observed in the present measurements.

3. THREE-BODY ATTACHMENT COEFFICIENT

Measurements of the three-body attachment coefficient have been determined over the range $0.6 \leq E/N \leq 30 \times 10^{-21}$ V·m^2. Since only a single negative-ion species is observed, the attachment coefficient may be determined from either the current or the charge waveforms; both methods have been shown to give the same value of η, to within the experimental uncertainty, at values of E/N where both methods can be conveniently used. However, at the lowest values of E/N, the large value of the attachment coefficient, which increases with decreasing E/N, is more conveniently determined directly from the slope of the semilog plot of the time-dependent ion-current component of the total anode waveform, as illustrated in Figure 9. For all waveforms analyzed using this method, the experimental points differ from the regression fit by less than ± 3%. In contrast, for values of E/N in the upper portion of the range investigated, the attachment coefficient becomes so small that its measurement is

more accurately determined from the charge waveforms. In order to maximize η via its quadratic density dependence, the maximum gas density is used. To do so within the voltage constraints of the drift tube, measurements have been made at the smaller drift distances, down to 0.7 cm. In this way it has been possible to determine values of η at values of E/N up to 3×10^{-20} V·m^2.

A summary of the values of the attachment coefficient is given in Table 5 and the data are compared with previous measurements (Refs. 9, 13, 24, and 25) in Figure 13. The present measurements have an estimated uncertainty of ± 5% and the values reported represent the mean of two or more measurements at each value of E/N, the spread being less than the specified uncertainty. Measurements carried out at different gas densities for a given value of E/N have established the quadratic dependence of the attachment coefficient on gas density.

The values of the attachment rate coefficient, summarized in Table 5, are obtained by combining the measurements of η/N^2 with the measurements of w_e. These values have an estimated uncertainty of ± 6%. These data are compared with previous measurements (Refs. 9, 13, and 26) in Figure 14 where the lower abscissa also shows the values of (3/2) eD_T/μ_e measured by Rees and Jory (Ref. 27) in dry, CO_2-free air to indicate the range of electron mean energy covered by the present measurements. Also shown in Figure 14 by the arrow on the left ordinate is the value of the three-body coefficient for thermal electrons deduced using recent measurements (Ref. 28) in oxygen and oxygen-nitrogen mixtures, i.e., from

$$k_a = 0.044\ k_1 + 0.166\ k_2 \qquad (31)$$

where k_1 and k_2 are the rate coefficients for oxygen and nitrogen as the third body, respectively, and a density ratio of nitrogen to oxygen of 79/21 has been assumed. Thus, using the values (Ref. 28) for $k_1 = 2.15 \times 10^{-42}$ m^6/s and $k_2 = 1 \times 10^{-43}$ m^6/s, gives a value of $k_a = 1.11 \times 10^{-43}$ m^6/s. The data shown in Figure 14 suggest that the attachment rate coefficient has a peak within the range of electron mean energy between thermal and 0.2 eV reflecting the peak found previously (Refs. 7 and 29) in pure oxygen. The present observation that the attachment rate coefficient does not vary appreciably

TABLE 5. VALUES OF THE THREE-BODY ATTACHMENT RATE IN DRY AIR

E/N 10^{-21} V·m^2	EN_o/N 10^4 V/m	$\nu_a(3)N_o^2/N^2$ 10^7/s	$\nu_a(3)/N^2$ 10^{-44} m^6/s
0.600	1.613	8.4	11.7
0.800	2.150	7.8	10.7
1.000	2.688	7.2	9.9
1.500	4.03	5.8	8.1
2.000	5.38	4.8	6.6
3.000	8.06	3.5	4.8
4.00	10.75	2.60	3.6
5.00	13.44	2.15	2.97
6.00	16.13	1.78	2.46
7.00	18.82	1.51	2.09
8.00	21.50	1.46	2.02
9.00	24.19	1.36	1.88
10.00	26.88	1.35	1.87
12.50	33.60	1.35	1.87
15.00	40.3	1.31	1.81
17.50	47.0	1.24	1.71
20.00	53.8	1.18	1.63
25.00	67.2	1.05	1.45
30.00	80.6	1.01	1.40

$N_o = 2.688 \times 10^{25}$ m^{-3}

Estimated uncertainties in the measured quantities are:

E/N: $\pm$ 0.2%

$\nu_a(3)/N^2$, $\nu_a(3)N_o^2/N^2$: $\pm$ 6%

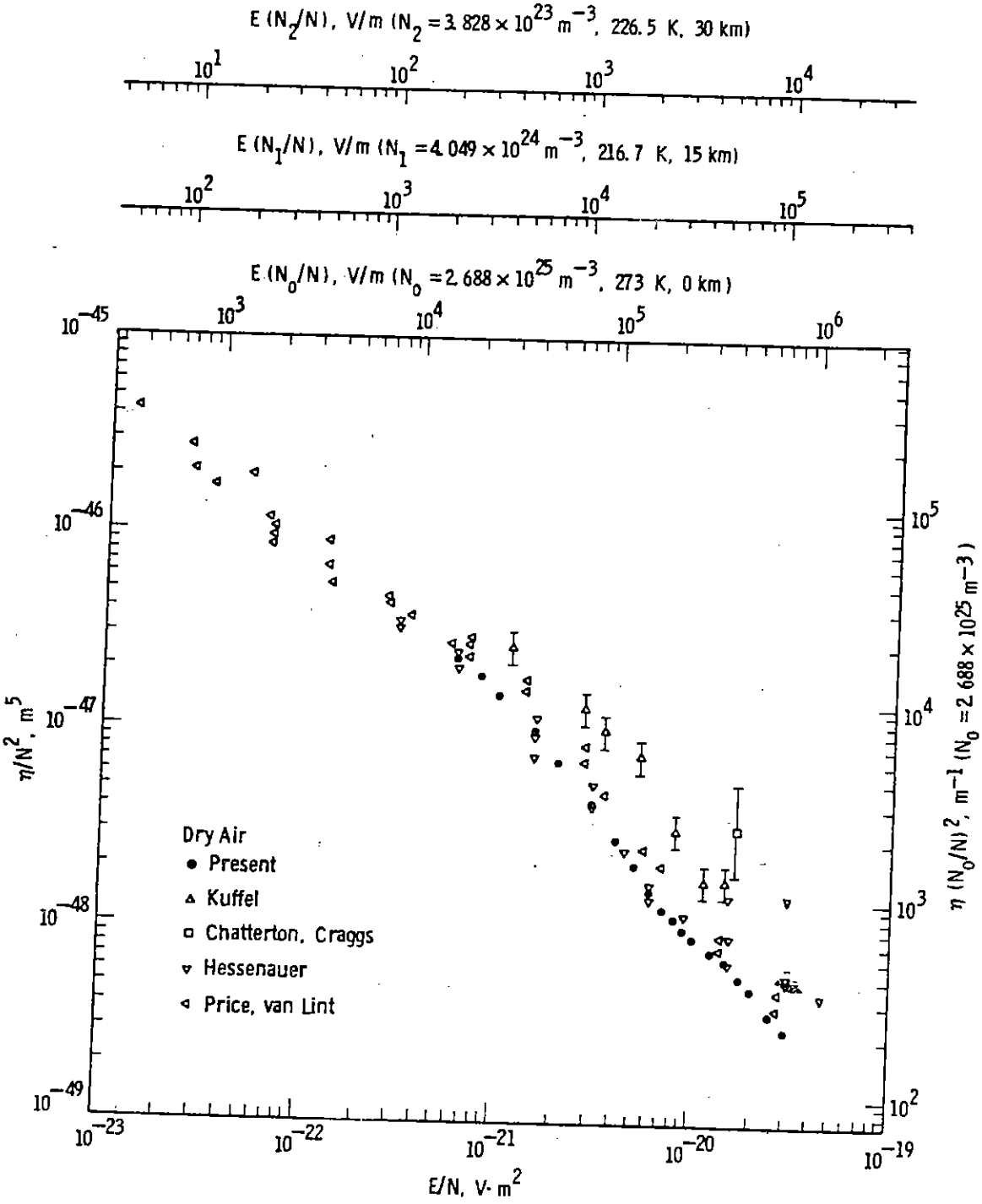

Figure 13. Comparison of the present measurements of the three-body attachment coefficient as a function of E/N with previous data.

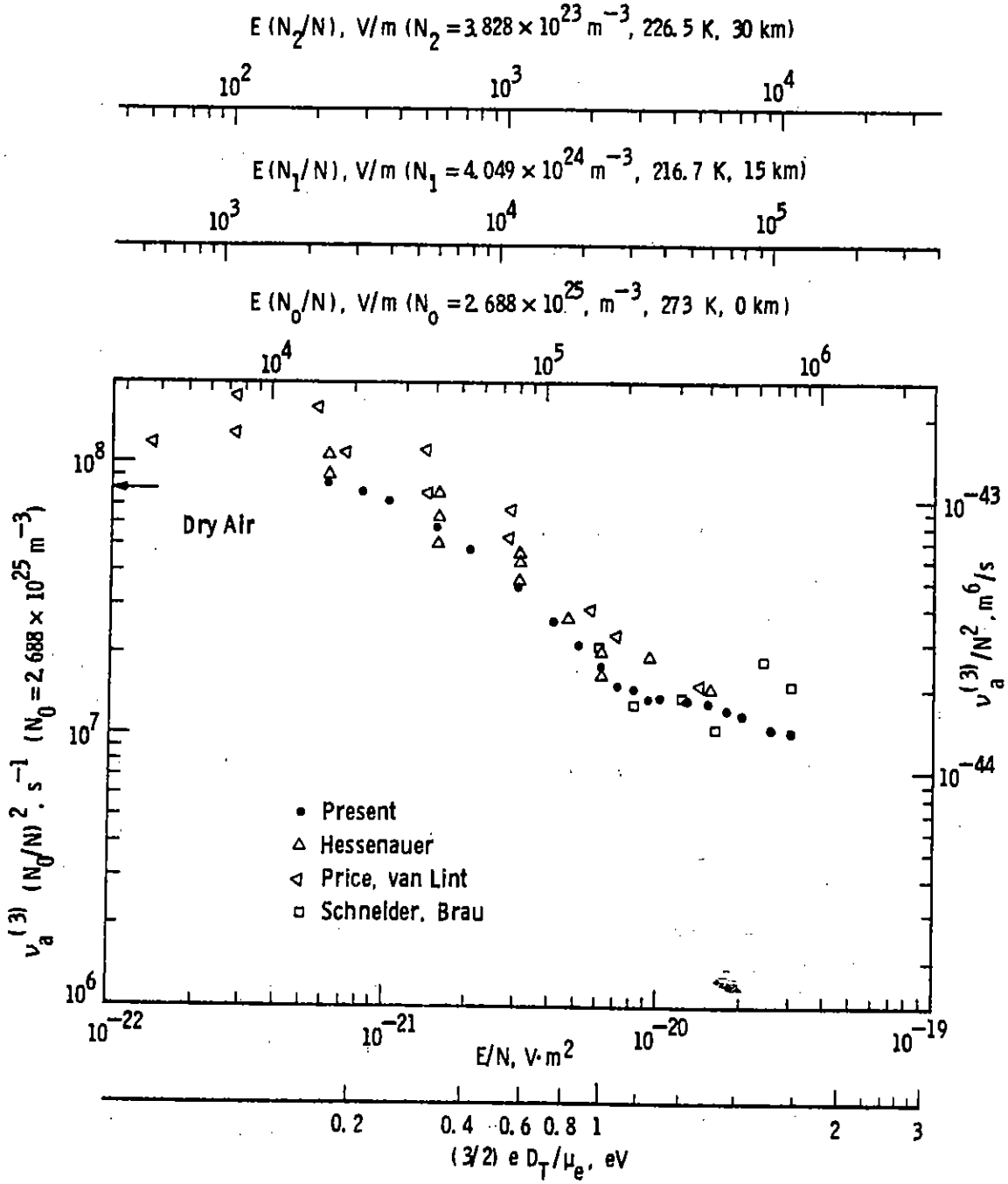

Figure 14. Comparison of the present measurements of the three-body attachment rate coefficient as a function of E/N with previous data. The arrow on the ordinate corresponds to the thermal value of the rate coefficient deduced from previous measurements (Ref. 28) in oxygen and oxygen-nitrogen mixtures.

with E/N over the range from 8 to 30 x 10^{-21} V•m^2 is consistent with the plateau region found (Ref. 27) in the measurements of D_T/μ_e over the same range of E/N. In this range of E/N, the electron mean energy is approximately constant as a result of the effective energy barrier introduced by the large vibrational cross section in N_2 occurring at an energy of 2.2 eV.

It may be seen from Figures 13 and 14 that the present data lie on the lower edge of the spread of the previous measurements. However, there is no evidence for a two-body attachment process in this range of E/N, in contrast to the results of Schneider and Brau (Ref. 26) who find a sharply increasing two-body coefficient with decreasing E/N. Results of measurements carried out at a value of E/N = 3 x 10^{-21} V•m^2 (corresponding to an electron mean energy ~ 0.6 eV) where a large density range from 3.2 x 10^{24} to 1.3 x 10^{25} m^{-3} can be covered, show that the values of attachment coefficient are precisely described by a three-body process. At this value of E/N an upper limit of 10^{-21} m^3/s can be placed on a possible two-body rate coefficient.

Using the same data at E/N = 3 x 10^{-21} V•m^2, an upper limit of 5 x 10^{-71} m^9/s is placed on the rate coefficient for a possible four-body process. This is more than three orders of magnitude smaller than that reported by Shimamari and Hatano (Ref. 30) for a four-body rate at thermal energy with O_2 as the fourth body and more than one order of magnitude smaller than that found by Goans and Christophorou (Ref. 31) for a four-body rate at an energy ~ 0.05 eV with N_2 as the fourth body. This indicates that the four-body rate coefficients decrease rapidly with electron mean energy above thermal. At present, the results of Goans and Christophorou provide the only convincing evidence for the existence of a four-body process. However, their rate coefficient for the N_2 four-body process is too small, even at an electron mean energy ~ 0.05 eV, to be significant at atmospheric density. In the case of the oxygen four-body process, the data presented by Shimamari and Hatano (Ref. 30) could equally well be interpreted by a much lower value (even zero) for the four-body rate coefficient. Thus, it is concluded that at atmospheric density the only four-body process that requires further consideration is the O_2 four-body process and then only for mean energies near thermal.

4. TWO-BODY ATTACHMENT AND IONIZATION COEFFICIENTS

In Section III.3 it has been noted that the primary negative ion formed in the range of $E/N \geq 60 \times 10^{-21}$ V·m^2 is O^- produced in a two-body, dissociative attachment reaction [Eq. (22)]. Moreover, it has been concluded from mobility measurements that the ions observed at these values of E/N are O_3^- formed from O^- via a three-body ion-molecule reaction [Eq. (23)]. It has also been proposed (Refs. 32-35) that O^- ions can combine with nitrogen molecules in a two-body associative detachment reaction to form N_2O, i.e.,

$$O^- + N_2 \rightarrow N_2O + e \qquad (32)$$

Alternatively, if the O^- ions are sufficiently energetic they can suffer two-body collisional detachment reactions with either nitrogen or oxygen molecules (Refs. 10 and 36-39) i.e.,

$$O^- + M \rightarrow O + M + e \qquad (33)$$

where M is either an oxygen or nitrogen molecule. Thus, for an arbitrary density N, the measured attachment coefficient is an effective coefficient which is a function of the true attachment coefficient (for O^- formation), the charge transfer coefficient, and the detachment coefficient (Ref. 40). Evidently, since the charge transfer reaction involving O^- is a three-body process, the effective attachment coefficient tends towards the true attachment coefficient with increasing gas density. In order to minimize detachment effects in the present study, measurements have been made at the maximum values of gas density consistent with electrical breakdown constraints, by working at small drift distances.

The values of the net ionization coefficient determined as a function of E/N from either the negative-ion or positive-ion waveforms are given in Table 6 and plotted as absolute values in Figure 15 where they are compared with previous measurements (Refs. 9, 25, and 41-45). For values of $E/N \leq 70 \times 10^{-21}$ V·m^2 no positive ions are detected and the data in this region correspond to pure attachment coefficients. In contrast to previous work (Refs. 44 and 45), negative ions are detected at values of $E/N > 100 \times 10^{-21}$ V·m^2,

TABLE 6. SUMMARY OF VALUES OF THE SWARM PARAMETERS IN DRY AIR

E/N 10^{-21} V·m^2	w_e m/s	μ_e m^2/V·s	μ_e* m^2/V·s	μ_- 10^{-4} m^2/V·s	μ_+ 10^{-4} m^2/V·s	$n^{(3)}/N^2$ 10^{-48} m^5	$k_a^{(3)}$ 10^{-44} m^6/s	$(\alpha-\eta)/N$ 10^{-22} m^2	α/η	$\eta^{(2)}/N$ 10^{-22} m^2	$k_a^{(2)}$ 10^{-18} m^3/s	α/N 10^{-22} m^2	k_i 10^{-18} m^3/s
0.100			0.949										
0.120			0.840										
0.140			0.757										
0.170			0.635										
0.200			0.569										
0.250			0.485										
0.300			0.429										
0.350			0.389										
0.400			0.360										
0.500			0.323										
0.600	4.95×10^3	0.307	0.296	2.28		23.6	11.7						
0.700	5.31×10^3	0.282											
0.800	5.68×10^3	0.264	0.262	2.27		18.9	10.7						
0.900	6.10×10^3	0.252											
1.000	6.58×10^3	0.245	0.236	2.28		15.1	9.9						
1.250	7.55×10^3	0.225											
1.500	8.09×10^3	0.201		2.27		10.0	8.1						
1.750	8.90×10^3	0.189											
2.000	9.53×10^3	0.177		2.28		6.9	6.6						
2.500	1.04×10^4	0.155											
3.000	1.12×10^4	0.139		2.27		4.3	4.8						
3.500	1.19×10^4	0.127											
4.00	1.27×10^4	0.118		2.27		2.83	3.6						
4.50	1.33×10^4	0.110											
5.00	1.41×10^4	0.105		2.26		2.11	2.97						
6.00	1.55×10^4	0.0961		2.27		1.59	2.46						
7.00	1.67×10^4	0.0887		2.28		1.25	2.09						
8.00	1.79×10^4	0.0832		2.28		1.13	2.02						
9.00	1.91×10^4	0.0789		2.28		0.99	1.88						
10.00	2.09×10^4	0.0777		2.28		0.90	1.87						
12.50	2.43×10^4	0.0723		2.27		0.77	1.87						
15.00	2.70×10^4	0.0670		2.27		0.67	1.81						
17.50	3.00×10^4	0.0638		2.27		0.57	1.71						
20.00	3.28×10^4	0.0610		2.28		0.50	1.63						
25.00	3.91×10^4	0.0582		2.27		0.36	1.45						
30.00	4.48×10^4	0.0556		2.28		0.31	1.40						
35.00	4.99×10^4	0.0530		2.27									
40.0	5.58×10^4	0.0519		2.27									
45.0	6.10×10^4	0.0504											
50.0	6.67×10^4	0.0496											
60.0	7.44×10^4	0.0461		3.03				$-0.069 \pm 5\%$		$0.069 \pm 5\%$	$0.51 \pm 6\%$		
70.0	8.44×10^4	0.0449		3.15				$-0.128 \pm 6\%$		$0.128 \pm 6\%$	$1.08 \pm 7\%$		
80.0	9.60×10^4	0.0446		3.22				$-0.115 \pm 7\%$	0.34	$0.174 \pm 8\%$	$1.67 \pm 9\%$	$0.059 \pm 8\%$	$0.57 \pm 9\%$
90.0	1.09×10^5	0.0451		3.29				$-0.091 \pm 8\%$	0.58	$0.217 \pm 10\%$	$2.4 \pm 11\%$	$0.126 \pm 12\%$	$1.37 \pm 13\%$
100.0	1.21×10^5	0.0450											
112.5	(1.34×10^5)†			3.27	2.54			$0.18 \pm 8\%$	1.76	$0.236 \pm 10\%$	$3.2 \pm 12\%$	$0.42 \pm 7\%$	$5.6 \pm 9\%$
125.0	1.46×10^5	0.0434		3.18	2.56			$0.48 \pm 3\%$	3.7	$0.178 \pm 5\%$	$2.6 \pm 7\%$	$0.66 \pm 4\%$	$9.6 \pm 6\%$
137.5	(1.56×10^5)†			3.06	2.57			$0.87 \pm 3\%$	7.9	$0.126 \pm 5\%$	$1.97 \pm 7\%$	$1.00 \pm 4\%$	$15.6 \pm 6\%$
150.0	1.68×10^5	0.0417		2.98	2.59			$1.37 \pm 3\%$	16.7	$0.087 \pm 5\%$	$1.46 \pm 7\%$	$1.46 \pm 4\%$	$24.5 \pm 6\%$
175.0	1.96×10^5	0.0417		2.85	2.55			$2.70 \pm 3\%$					‡ 55 5%
200.0	2.19×10^5	0.0407			2.50			$4.6 \pm 3\%$					‡101 5%
225.0	(2.37×10^5)†				2.43			$7.3 \pm 3\%$					‡173 5%
250.0	2.52×10^5	0.0375			2.35			$10.2 \pm 3\%$					‡257 5%
275.0	(2.73×10^5)†				2.27			$12.8 \pm 3\%$					‡349 5%
300.0	2.95×10^5	0.0366			2.21			$17.0 \pm 3\%$					‡502 5%

* Data of Hegerberg and Reid (Ref. 14)

† Extrapolated value

‡ Net ionization rate coefficient

Thermal μ_e: 1.61 m^2/V·s(Ref. 15, 16); 1.75 m^2/V·s(Ref. 17)

Thermal $k_a^{(3)}$: 1.11×10^{-43} m^6/s (Ref. 28)

Estimated uncertainties in the measured quantities are:

E/N: $\pm$ 0.2%

w_e, μ_e: $\pm$ 1% for E/N $\leq 10^{-19}$ V·m^2; $\pm$ 2% for E/N > 10^{-19} V·m^2

μ_-, μ_+: $\pm$ 1%

$n^{(3)}/N^2$: $\pm$ 5%

$k_a^{(3)}$: $\pm$ 6%

α/η: $\pm$ 2%

$(\alpha-\eta)/N$, $\eta^{(2)}/N$, $k_a^{(2)}$, α/N, k_i: As noted in table

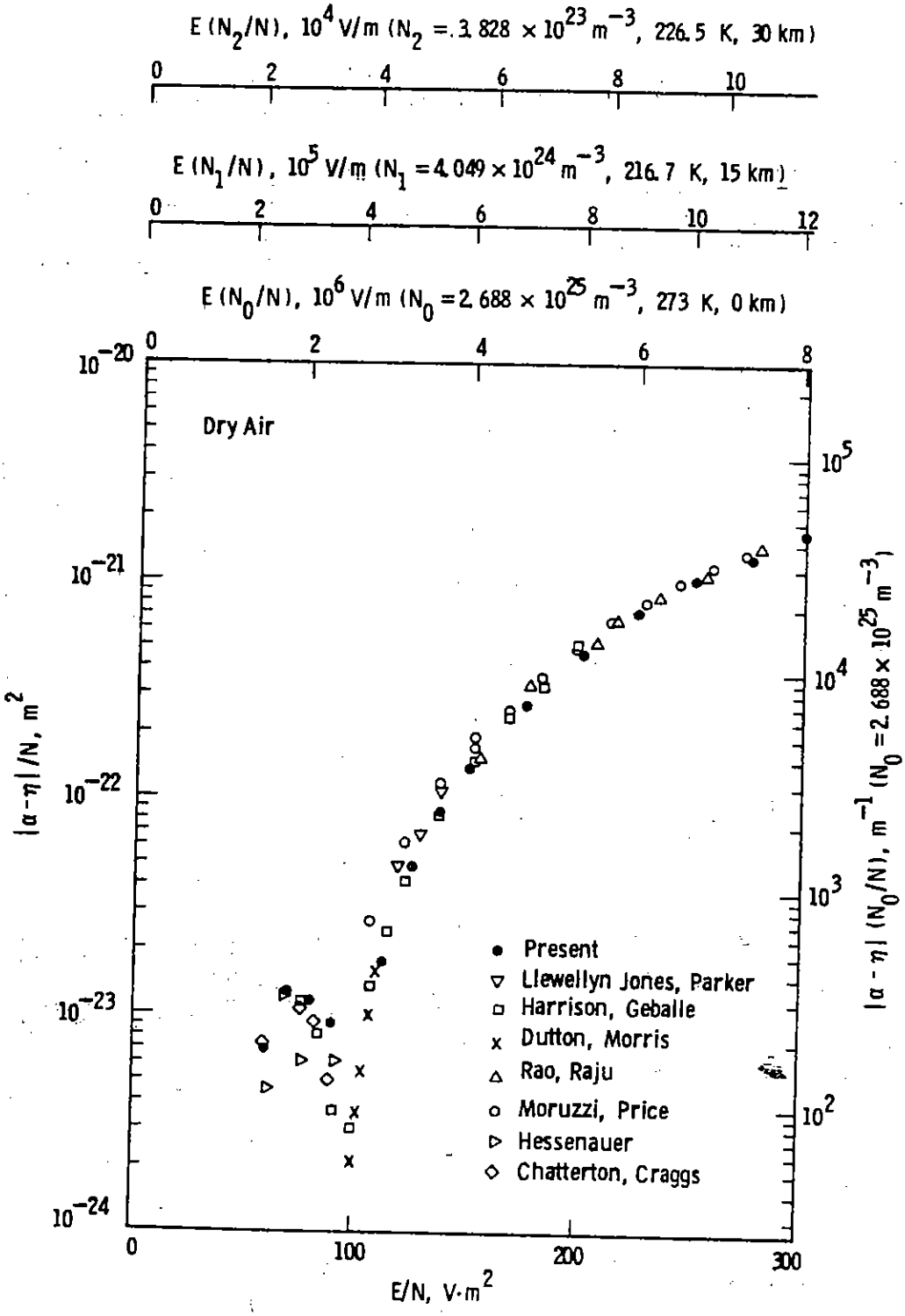

Figure 15. Comparison of the present values (solid points) of the net ionization coefficient as a function of E/N with previous measurements.

i.e., well above the onset of ionization. The estimated uncertainty in the present measurements is given at each value of E/N in Table 6.

From Figure 15 it is seen that the present measurements lie on the lower edge of the spread in the previous data. The largest spread among the different measurements occurs in the region of the limiting value of E/N and is attributed to a combination of the increasing measurement uncertainty at values of E/N approaching the limiting value (cf. Section III.6) and the effects due to electron detachment which become more apparent in the region of E/N where $\alpha \approx \eta$.

The present measurements of α/η which are given in Table 6 have been determined directly from the ratio of the positive charge to negative charge collected as discussed in Section II.4, i.e., neglecting detachment effects. The estimated uncertainty in this ratio is ± 2%. Combining these measurements with the values of the net ionization coefficient and using the values of w_e given in Table 2 gives the rate coefficients for two-body attachment and ionization shown in Figure 16 and in Tables 7 and 8. The data for the individual coefficients are confined to values of E/N < 150 x 10^{-21} V•m^2 for which sufficiently high gas densities can be used to minimize detachment effects. For higher values of E/N the data correspond to net ionization rates.

The influence of detachment on the present values of two-body attachment and ionization rates is difficult to assess. Measured rate coefficients that have been reported for associative detachment vary by more than one order of magnitude whereas those for collisional detachment vary by more than three orders of magnitude. Moreover, the onset for associative detachment occurs at a value of E/N ~ 5 x 10^{-21} V•m^2, whereas that for collisional detachment occurs at E/N ~ 100 x 10^{-21} V•m^2. For values of E/N < 100 x 10^{-21} V•m^2, the present values of $\nu_a^{(2)}$ are in good agreement with those predicted (Ref. 46) from solutions to the Boltzmann transport equation using cross sections for oxygen and nitrogen, appropriately weighted to reflect the relative concentrations of the air constituents, and neglecting detachment. This agreement is taken as evidence that associative detachment is not important, at least at the gas densities used for the present measurements. On the other hand, the decrease in $\nu_a^{(2)}$ with increasing E/N observed for values of E/N >

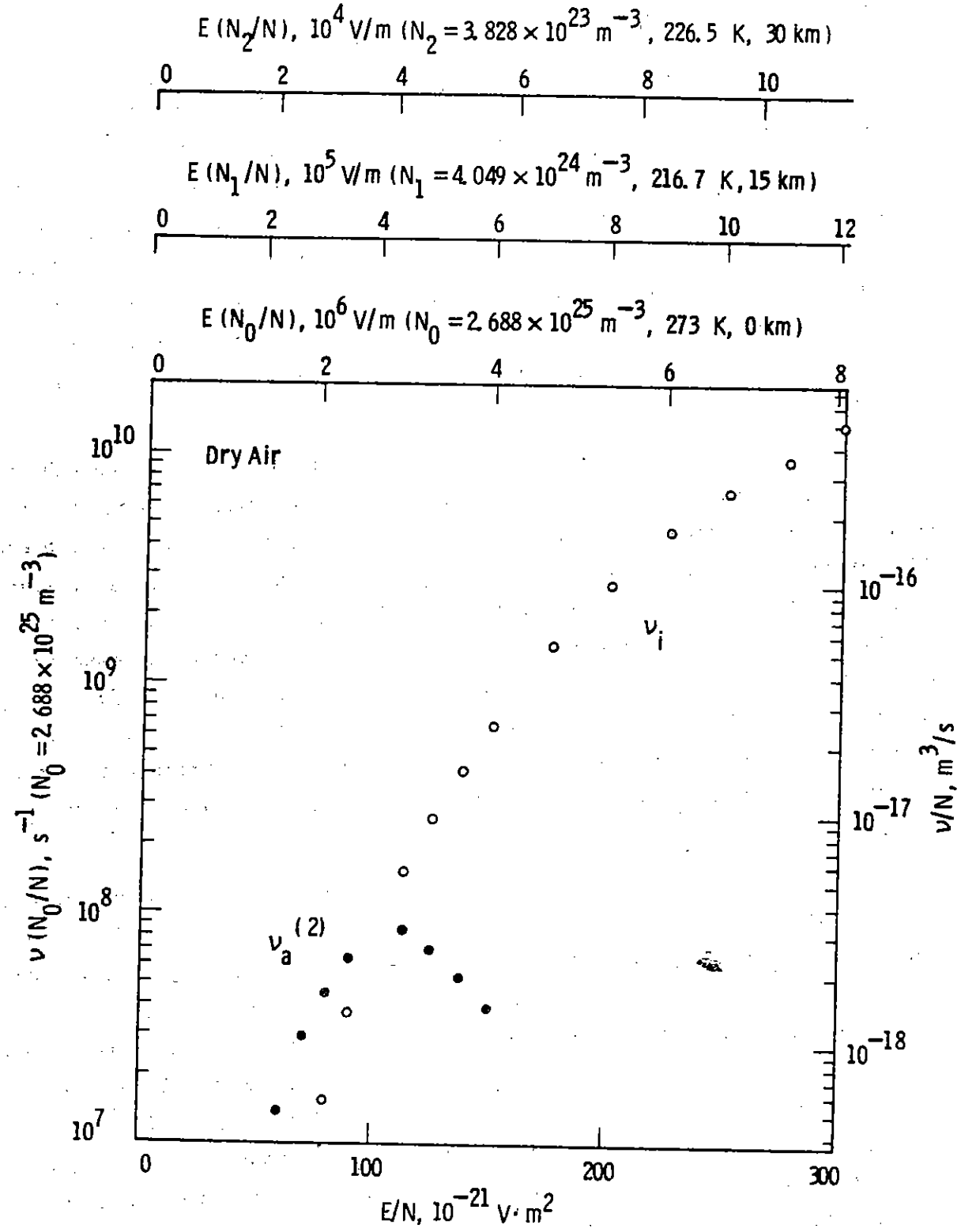

Figure 16. Present measurements of the two-body attachment rate coefficient (solid points) and ionization rate coefficient (open points) as a function of E/N.

TABLE 7. VALUES OF THE TWO-BODY ATTACHMENT RATE IN DRY AIR

N 10^{22} m^{-3}	E/N 10^{-21} $V \cdot m^2$	EN_o/N 10^4 V/m	$\nu_a^{(2)} N_o/N$ $10^7/s$	$\nu_a^{(2)}/N$ 10^{-18} m^3/s
265	60.0	161.3	1.37 ± 6%	0.51 ± 6%
133	70.0	188.2	2.9 ± 7%	1.08 ± 7%
133	80.0	215.0	4.5 ± 9%	1.67 ± 9%
133	90.0	241.9	6.4 ± 11%	2.4 ± 11%
66.6	112.5	302.4	8.5 ± 12%	3.2 ± 12%
30.6	125.0	336.0	7.0 ± 7%	2.6 ± 7%
25.8	137.5	369.6	5.3 ± 7%	1.97 ± 7%
19.4	150.0	403	3.9 ± 7%	1.46 ± 7%

$N_o = 2.688 \times 10^{25}$ m^{-3}

Estimated uncertainties in the measured quantities are:

E/N: ± 0.2%

$\nu_a^{(2)}/N$, $\nu_a^{(2)} N_o/N$: As noted in table

TABLE 8. VALUES OF THE IONIZATION RATE IN DRY AIR

N 10^{22} m^{-3}	E/N 10^{-21} $V \cdot m^2$	EN_o/N 10^4 V/m	$\nu_i N_o/N$ 10^7/s	ν_i/N 10^{-18} m^3/s
133	80.0	215.0	1.53 ± 9%	0.57 ± 9%
133	90.0	241.9	3.7 ± 13%	1.37 ± 13%
66.6	112.5	302.4	15.1 ± 9%	5.6 ± 9%
30.6	125.0	336.0	26 ± 6%	9.6 ± 6%
25.8	137.5	369.6	42 ± 6%	15.6 ± 6%
19.4	150.0	403	66 ± 6%	24.5 ± 6%
6.54	175.0	470	148 ± 5%	‡ 55 ± 5%
6.54	200.0	538	271 ± 5%	‡101 ± 5%
6.54	225.0	605	465 ± 5%	‡173 ± 5%
3.35	250.0	672	690 ± 5%	‡257 ± 5%
1.71	275.0	739	940 ± 5%	‡349 ± 5%
1.71	300.0	806	1350 ± 5%	‡502 ± 5%

$N_o = 2.688 \times 10^{25}$ m^{-3} ‡ Net ionization rate coefficient

Estimated uncertainties in the measured quantities are:

E/N: ± 0.2%

ν_i/N, $\nu_i N_o/N$: As noted in table

100×10^{-21} V•m^2 is not predicted from solutions to the Boltzmann equation. This may indicate the presence of collisional detachment and that for E/N > 100×10^{-21} V•m^2 the present measurements should be regarded as effective values. For this reason, the values of gas density at which the measurements were made have been included in Tables 7 and 8. However, it is pointed out that for values of E/N > 200×10^{-21} V•m^2 attachment is so small (< 5%) compared to ionization that the presently reported values of the ionization rate should be insensitive to detachment effects. Future measurements in mixtures of dry air and water vapor are expected to provide additional information on the importance of detachment in this region of E/N by virtue of the additional channel for stable-ion formation that is available through clustering reactions between O^- and water vapor molecules [Eq. (27)].

5. DISCUSSION

The present data represent a comprehensive set of measurements of the swarm parameters in dry air and will serve as a base for future measurements in dry air-water vapor mixtures. The complete data base for dry air determined in the present study is summarized in Table 6. Also included in Table 6 are the values of electron mobility measured by Hegerberg and Reid (Ref. 14) over the range from 0.1 to 1 $\times 10^{-21}$ V•m^2, which represent the most reliable data currently available at values of E/N below the lower limit of the present measurements.

A plot of the three-body and two-body attachment frequencies together with the ionization frequency corresponding to atmospheric density at 0 km and 273K (2.688×10^{25} m^{-3}) is shown in Figure 17. Extrapolating the data on the three-body attachment frequency to higher values of E/N, it appears that the two-body attachment frequency is at least an order of magnitude larger than the three-body attachment frequency in the vicinity of the limiting value of E/N. On this basis, for gas densities up to atmospheric density, observed (Ref. 47) departures from Paschen's Law are more likely due to the variation with gas density of the branching ratio of the reaction channels of the O^- ions (i.e., stable ion formation versus detachment) rather than the influence of three-body attachment.

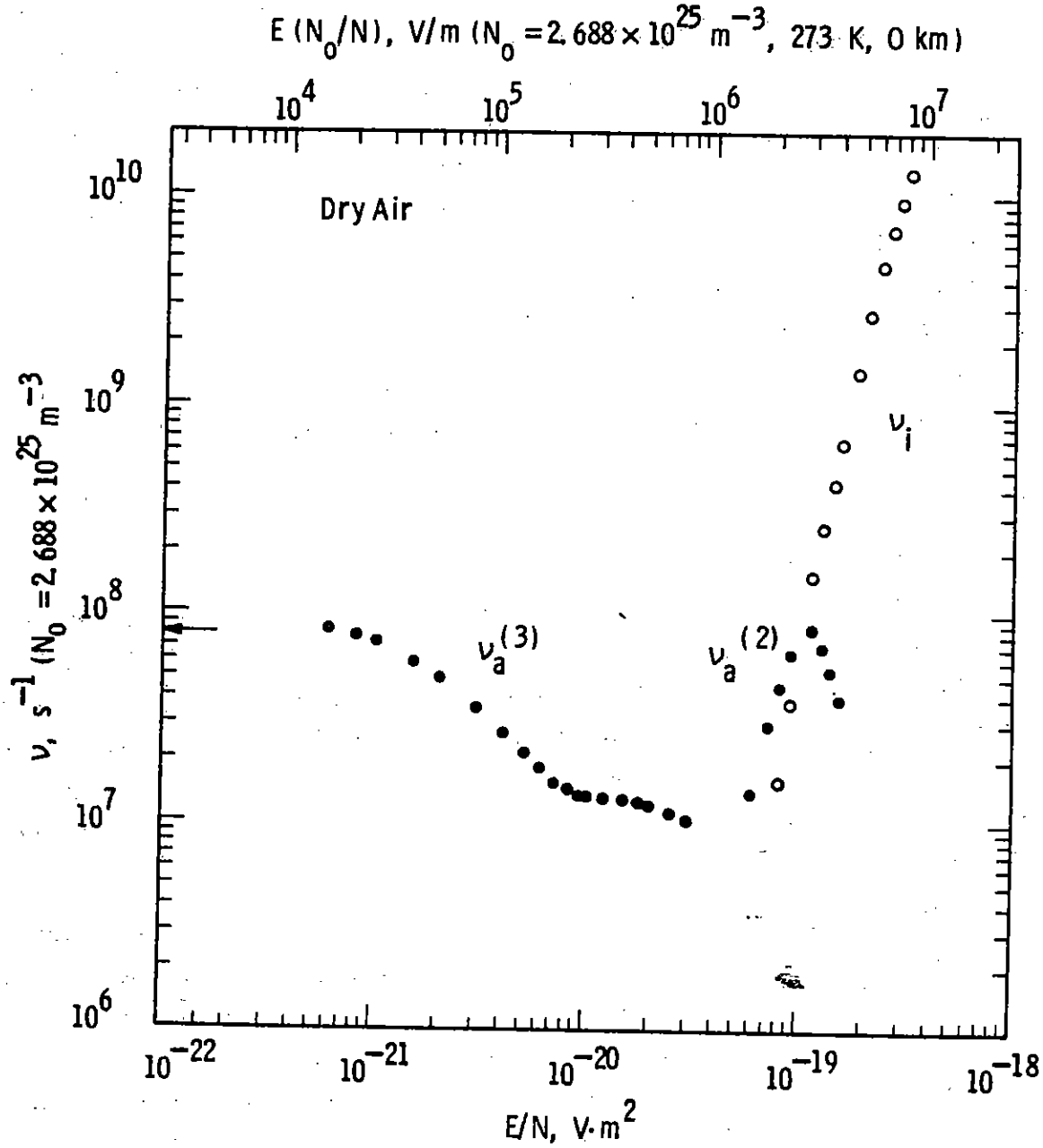

Figure 17. Present measurements of the attachment and ionization frequencies normalized to atmospheric density at 0 km and 273 K ($N_o = 2.688 \times 10^{25}$ m^{-3}) as a function of E/N. The arrow on the ordinate corresponds to the thermal value of $\nu_a(3)$ deduced from previous measurements (Ref. 28).

6. ESTIMATES OF MEASUREMENT UNCERTAINTIES

The values determined for the swarm parameters are subject to both random errors arising from the statistical variations in the measured current waveforms and systematic errors arising from uncertainties in the absolute values of E, N and t. The magnitudes of these uncertainties depend both on the particular swarm parameter and on the functional dependence of that parameter with E/N.

The absolute values of E, N, and t are each determined with an uncertainty of ± 0.1% and so an overall uncertainty of ± 0.2% is assigned to the values of E/N. Describing the local functional dependence of a swarm coefficient on E/N by $(E/N)^n$, the uncertainty in the coefficient due to the uncertainty in E/N is given by

$$\Delta(\text{coefficient})/\text{coefficient} = n\,\Delta(E/N)/(E/N) = \pm\, 0.2\ n\% \qquad (34)$$

a. Electron Mobility

The values of the electron drift velocity are determined from the slope of plots of τ_e versus d. In the present work, for values of $E/N \leq 10^{-19}$ V·m^2, the slope is determined to ± 0.5%, while for values of $E/N > 10^{-19}$ V·m^2 the uncertainty increases to ± 1% due to the smaller electron transit times. From Figure 10, it is seen that $n \leq 1$ so that from Equation (34) the uncertainty in w_e due to uncertainty in setting E/N is ≤ ± 0.2%. Thus, the assigned overall uncertainty limits in w_e or μ_e are ± 1% for $E/N \leq 10^{-19}$ V·m^2 and ± 2% for $E/N > 10^{-19}$ V·m^2. These uncertainty limits do not include corrections due to attachment and ionization effects. From Equation (3), this correction is $200(D_L/\mu_e)(\alpha - \eta)/E$ % and is positive when $\alpha > \eta$ and negative when $\eta > \alpha$. At low values of E/N ($\alpha = 0$), η/E increases with decreasing E/N while D_L/μ_e decreases with decreasing E/N, i.e., to a degree the two component factors are compensating. In addition, since the attachment occurs by a three-body process the value of η/E may be kept small by a suitable choice of gas density. At large values of E/N where $\alpha > \eta$, both $(\alpha - \eta)/E$ and D_L/μ_e are monotonically increasing functions of E/N so that the correction increases with increasing E/N. Based on available knowledge of D_L/μ_e, α/E, and η/E the corrections to the present measurements are less than 0.5% for $E/N \leq 2 \times 10^{-19}$

$V \cdot m^2$ but may increase to 2% at a value of $E/N = 3 \times 10^{-19}$ $V \cdot m^2$. Since the corrections are less than the assigned uncertainties in the values of w_e (or μ_e), no corrections have been applied to the reported values.

b. Ion Mobility

The values of the ion drift velocity $w_\pm$ are determined from the slope of plots of $\tau_\pm$ versus d, respectively. In the present work, the slope of such plots is determined to ± 0.5%. From Figure 12, it is seen that $n \sim 1$ so that from Equation (34) the uncertainty in $w_\pm$ due to the uncertainty in setting E/N is ~ ± 0.2%. Thus, the assigned overall uncertainty in $w_\pm$ or $\mu_\pm$ is ± 1%.

c. Three-Body Attachment Coefficient

From the analysis of negative ion current waveforms measured in the present study, the slope $\eta^{(3)}w_-$ of plots of $\ell n\ I_-(d,t)$ versus t is determined to ± 3%. Using the measured values of w_- (which have an estimated uncertainty of ± 1%) results in an uncertainty of ± 4% in the values of $\eta^{(3)}$. From Figure 13, the value of n in Equation (34) varies from 0.8 to 1.6 over the range of the present measurements so that the uncertainty in $\eta^{(3)}/N^2$ due to the uncertainty in setting E/N is less than ± 0.4%. Thus, an overall uncertainty of ± 5% is assigned to the values of $\eta^{(3)}/N^2$ and of ± 6% to the values of k_a using the previously measured values of w_e of estimated uncertainty ± 1%.

d. Net Ionization Coefficient

The values of $\exp(\alpha-\eta)\Delta d$ given by the slope of plots of $y^C_{d+\Delta d}$ versus y^C_d have an uncertainty of ± 1%. The uncertainty in the value of $(\alpha-\eta)$ resulting from the uncertainty in the slope is given by

$$\Delta(\alpha-\eta)/(\alpha-\eta) = \{1/[(\alpha-\eta)\Delta d]\}\Delta(\text{slope})/\text{slope} \qquad (35)$$

In the present measurements, for values of $E/N \geq 125 \times 10^{-21}$ $V \cdot m^2$, $(\alpha-\eta)\Delta d > 0.5$, so that an uncertainty of ± 2% is assigned to the uncertainty of $(\alpha-\eta)$ determined from the slope of the integrated current plots. From plots of $\ell n\ [(\alpha-\eta)/N]$ versus $\ell n(E/N)$, n in Equation (34) varies from 6 at low E/N to 2.5 at high E/N resulting in an uncertainty in $(\alpha-\eta)/N$ as a result of uncertainty

in setting E/N of less than ± 1.2%. Thus, an overall uncertainty of ± 3% is assigned to the values of $(\alpha-\eta)/N$ for $E/N > 125 \times 10^{-21}$ V·m^2. For lower values of E/N, the uncertainties increase as $\alpha/\eta^{(2)}$ approaches unity. Estimates of the uncertainties in $(\alpha-\eta)/N$ for $E/N < 125 \times 10^{-21}$ V·m^2 are as noted in Table 6.

e. Two-Body Attachment and Ionization Coefficients

The ratio of $\alpha/\eta^{(2)}$ is determined from measurements of the ratio $(Q_+^C/Q_o)/(Q_-^A/Q_o)$ with an estimated uncertainty of ± 2%. The values of α/N and $\eta^{(2)}/N$ are then determined, using the measured values of $(\alpha-\eta)$ from

$$\alpha/N = [(\alpha-\eta)/N]/(1-\eta^{(2)}/\alpha) \tag{36}$$

$$\eta^{(2)}/N = [(\alpha-\eta)/N]/(\alpha/\eta^{(2)}-1) \tag{37}$$

Thus, estimates of the uncertainties in α/N and $\eta^{(2)}/N$ depend on the magnitude of $\alpha/\eta^{(2)}$. In particular, even if the net ionization coefficient and the ratio of the coefficients are determined reasonably precisely, large uncertainties arise in both coefficients when $\alpha/\eta^{(2)}$ approaches unity. Estimates of the uncertainties in α/N, k_i, $\eta^{(2)}/N$, and $k_a^{(2)}$ are given in Tables 6, 7, and 8 at each value of E/N. These estimates do not include uncertainties due to the effects of detachment.

REFERENCES

1. Manufactured by Buckbee-Mears Company.

2. MKS Instruments, Inc.

3. D. Stelman, J. L. Moruzzi, and A. V. Phelps, "Low Energy Electron Attachment to Ozone using Swarm Techniques," J. Chem. Phys. 56, 4183-4189, (1972).

4. P. J. Chantry, D. K. Davies and G. W. Sherwin, "Data Acquisition Scheme for Cancellation of Time Dependent Background Signals and Design of an Optical Absorption Cell for Monitoring Water Vapor in Air," Dikewood, Division of Kaman Sciences Corporation Report No. DC-TN-1506-7, August 1981.

5. G. S. Hurst, L. B. O'Kelly, E. B. Wagner, and J. A. Stockdale, "Time-of-Flight Investigations of Electron Transport in Gases," J. Chem. Phys. 39, 1341-1345, (1963).

6. J. Lucas, "The Amplification and Transit Time of an Electron Avalanche Traversing a Uniform Electric Field Gap," Int. J. Electron. 17, 43-48, (1964).

7. L. M. Chanin, A. V. Phelps, and M. A. Biondi, "Measurements of the Attachment of Low-Energy Electrons to Oxygen Molecules," Phys. Rev. 128, 219-230, (1962).

8. R. A. Nielsen and N. E. Bradbury, "Electron and Negative Ion Mobilities in Oxygen, Air, Nitrous Oxide and Ammonia," Phys. Rev. 51, 69-75, (1937).

9. H. Hessenauer, "Anlagerungskoeffizienten und Driftgeschwindikeiten von Elektronen in Luft," Z. Phys. 204, 142-154, (1967).

10. L. Frommhold, "Uber verzogerte Elektronen in Elektronenlawinen, insbesondere in Sauerstoff und Luft, durch Bildung und Zerfall negativer Ionen (O^-)," Fortschr. Phys. 12, 597-642, (1964).

11. H. Ryzko, "Drift Velocity of Electrons and Ions in Dry and Humid Air and in Water Vapor," Proc. Phys. Soc. (Lond.), 85, 1283-1295, (1965).

12. J. A. Rees, "Electron Drift Velocities in Air," Aust. J. Phys. 26, 427-431, (1963). Additional data obtained in this study are presented in L.G.H. Huxley and R. W. Crompton, The Diffusion and Drift of Electrons in Gases (Wiley and Sons, 1974).

13. M. L. Price and V. A. J. van Lint, "Measurement of Electron Attachment and Mobility in Dry and Wet Air," Defense Nuclear Agency Report No. DNA 4788T, 1978 and Theoretical Note 342. The original data given in this report have since been revised and the corrected values appear in E. Pettus and W. F. Crevier, "Analytic Representation of Electron Mobility and Attachment Data in Dry and Moist Air from van Lint's HIFX Experiments," Mission Research Corporation Report No. MRC-R-576, 1980. The data plotted in Figures 11, 12, and 14 correspond to the revised values. See also V. A. J. van Lint, "Electron Mobility and Attachment in Dry and Moist Air," Defense Nuclear Agency Report No. DNA 6109T, 1982 and Theoretical Note 345.

14. R. Hegerberg and I. D. Reid, "Electron Drift Velocities in Air," Aust. J. Phys. 33, 227-230, (1980).

15. M. H. Mentzoni, "Momentum Transfer Collisions in Oxygen for Thermal Electrons," J. Res. Natl. Bur. Std. (U.S.), 69D, 213-217, (1965).

16. M. H. Mentzoni and R. V. Row, "Rotational Excitation and Electron Relaxation in Nitrogen," Phys. Rev. 130, 2312-2316, (1963).

17. H. B. Milloy, I. D. Reid, and R. W. Crompton, "Zero-field Mobility for Electrons in Dry and Humid Air," Aust. J. Phys. 28, 231-234, (1975).

18. J. L. Moruzzi and A. V. Phelps, "Survey of Negative-Ion-Molecule Reactions in O_2, CO_2, H_2O, CO, and Mixtures of these Gases at High Pressure," J. Chem. Phys. 45, 4617-4627, (1966).

19. D. A. Parkes, "Electron Attachment and Negative Ion-Molecule Reactions in Pure Oxygen," Trans. Faraday Soc. 67, 711-729, (1971).

20. F. C. Fehsenfeld and E. E. Ferguson, "Laboratory Studies of Negative Ion Reactions with Atmospheric Trace Constituents," J. Chem. Phys. 61, 3181-3193, (1974).

21. F. C. Fehsenfeld, E. E. Ferguson, and D. K. Bohme, "Additional Flowing Afterglow Measurements of Negative Ion Reactions of D-Region Interest," Planet. Space Sci. 17, 1759-1762, (1969).

22. M. T. Elford and J. A. Rees, "The Mobility of Negative Ions in Oxygen (293K)," Aust. J. Phys. 27, 333-355, (1974).

23. I. Dotan, J. A. Davidson, G. E. Streit, D. L. Albritton, and F. C. Fehsenfeld, "A Study of the Reaction $O_3^- + CO_2 \rightarrow CO_3^- + O_2$ and its Implication on the Thermochemistry of CO_3 and O_3 and their Negative Ions," J. Chem. Phys. 67, 2874-2879, (1977).

24. E. Kuffel, "Electron Attachment Coefficients in Oxygen, Dry Air, Humid Air and Water Vapour," Proc. Phys. Soc. (Lond.), 74, 297-308, (1959).

25. P. A. Chatterton and J. D. Craggs, "Attachment Coefficient Measurements in Carbon Dioxide, Carbon Monoxide, Air, and Helium-Oxygen Mixtures," Proc. Phys. Soc. (Lond.), 85, 355-362, (1965).

26. B. I. Schneider and C. A. Brau, "Two- and Three-Body Electron Attachment in Air," J. Phys. B 15, 1601-1607, (1982).

27. J. A. Rees and R. L. Jory, "The Diffusion of Electrons in Dry, Carbon Dioxide Free Air," Aust. J. Phys. 17, 307-314, (1964).

28. R. W. Crompton, R. Hegerberg, and H. R. Skullerud, "Diffusion, Attachment and Attachment Cooling of Thermal Electrons in Molecular Oxygen," Proc. International Seminar on Swarm Experiments in Atomic Collision Research, Tokyo, p. 18-22, (1979).

29. J. L. Pack and A. V. Phelps, "Electron Attachment and Detachment. I. Pure O_2 at Low Energy," J. Chem. Phys. 44, 1870-1883, (1966).

30. H. Shimamori and Y. Hatano, "Mechanism of Thermal Electron Attachment in O_2-N_2 Mixtures," Chem. Phys. 12, 439-445, (1976).

31. R. E. Goans and L. G. Christophorou, "Attachment of Slow (< 1 eV) Electrons to O_2 in Very High Pressures of Nitrogen, Ethylene, and Ethane," J. Chem. Phys. 60, 1036-1045, (1974).

32. J. Comer and G. J. Schulz, "Measurements of Electron Detachment Cross Sections from O^- and S^-," Phys. Rev. A 10, 2100-2106, (1974).

33. W. Lindinger, D. L. Albritton, F. C. Fehsenfeld, and E. E. Ferguson, "Reactions of O^- with N_2, N_2O, SO_2, NH_3, CH_4, and C_2H_4 and $C_2H_2^-$ with O_2 from 300°K to Relative Kinetic Energies of ~ 2 eV," J. Chem. Phys. 63, 3238-3242, (1975).

34. S. W. Rayment and J. L. Moruzzi, "Electron Detachment Studies between O^- Ions and Nitrogen," Int. J. Mass Spec. Ion Phys. 26, 321-326, (1978).

35. C. Doussot, F. Bastien, E. Marode, and J. L. Moruzzi, "A New Technique for Studying Ion Conversion and Detachment Reactions in Oxygen and in O_2/SO_2 and O_2/N_2 Mixtures," J. Phys. D 16, 2451-2461, (1982).

36. H. Ryzko and E. Astrom, "Electron Attachment-Detachment Processes in Dry Air," J. Appl. Phys. 38, 328-330, (1967).

37. M. J. Eccles, B. C. O'Neill, and J. D. Craggs," Electron Detachment in Oxygen," J. Phys. B 3, 1724-1731, (1970).

38. B. C. O'Neill and J. D. Craggs, "Collisional Detachment and Ion Molecule Reactions in Oxygen," J. Phys. B 6, 2625-2633, (1973).

39. G. Berger, "Collisional Detachment Lifetime of Negative Ions in Atmospheric Air," Proc. XV Int. Conf. Phen. Ionized Gases, Minsk, p. 571-572, (1981).

40. D. K. Davies, "Analysis of Current Growth Measurements in Attaching Gases," J. Appl. Phys. 47, 1916-1919, (1976).

41. F. Llewellyn-Jones and A. B. Parker, "Electrical Breakdown of Gases I. Spark Mechanism in Air," Proc. Roy. Soc. (Lond.) A213, 185-202, (1952).

42. M. A. Harrison and R. Geballe, "Simultaneous Measurement of Ionization and Attachment Coefficients," Phys. Rev. 91, 1-7, (1953).

43. J. Dutton and W. T. Morris, "The Mechanism of the Electrical Breakdown of Air in Uniform Fields at Voltages up to 400 kV," Brit. J. Appl. Phys. 18, 1115-1120, (1967).

44. C. Raja Rao and G. R. Govinda Raju, "Growth of Ionization Currents in Dry Air at High Values of E/N," J. Phys. D 4, 494-503, (1971).

45. J. L. Moruzzi and D. A. Price, "Ionization, Attachment and Detachment in Air and Air-CO_2 Mixtures," J. Phys. D 7, 1434-1440, (1974).

46. L. E. Kline, private communication.

47. O. Farish and D. J. Tedford, "Similarity in Air and Nitrogen I. Breakdown Voltages," J. Phys. D 2, 1555-1558, (1969).